ESA Climate Space Tipping Elements Project

SIRENE

Satellite Information for Resilience monitoring and Early warning of ecosystem tipping points

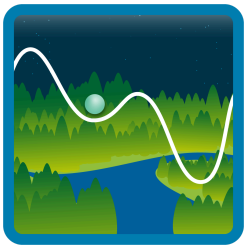

Inventory of Data and Tools to Analyse Vegetation Resilience
Deliverable D1.2

Authors: Maria C. Caldeira, Lana Blaschke, Ruxandra-Maria Zotta, Sebastian Bathiany
Contributing authors: Nicolas Bader, Ana Bastos, Niklas Boers, Manuel Campagnolo, Chan Diao, Wouter Dorigo, Tiago Ermitão, Teng Liu, Miguel Mahecha, Harry Morris, Bernardo Mota, Rasma Ormane, Roland Pail, José Cardoso Pereira, Zhen Qian, Danielle Rudley, Ana Russo, Cornelius Senf, João M. N. Silva, Taylor Smith, Steve Teo, Nils Voß, Sara Walcher, Xiaona Wang, Sophie Wolf

Version 1.1
March 3, 2026

TU WIEN NPL National Physical Laboratory UNIVERSITÄT LEIPZIG INSTITUTO SUPERIOR DE AGRONOMIA Universidade de Lisboa

DELIVERABLE TASK 1.2

INVENTORY OF DATA AND TOOLS TO ANALYSE VEGETATION RESILIENCE

Monitoring vegetation resilience is a pressing challenge in the context of climate and land-use change, as it is critical for assessing ecosystem health and anticipating potential regime shifts. Recent studies have investigated vegetation resilience using a wide range of datasets, indicators, and methodologies, but the resulting picture remains heterogeneous and fragmented. To advance towards a systematic understanding, it is essential to identify consistencies, resolve discrepancies, and address key knowledge gaps.

Within the framework of the SIRENE project, this effort focuses on compiling and assessing the most relevant observational datasets for resilience research. Building on recent advances and existing initiatives such as the ESA Climate Change Initiative (CCI), the project aims to establish a robust basis for satellite-based monitoring of vegetation resilience. Particular emphasis is placed on selecting meaningful vegetation indicators, developing resilience metrics suitable for large-scale applications, and benchmarking them against ground-based observations.

This document presents the inventory of datasets compiled in Task T1, which is organized into three main categories: ecosystem variables (e.g., vegetation, biomass, land cover, tree-ring data), drivers of vegetation dynamics (e.g., climate, disturbances), and tools (e.g., resilience metrics and models). The datasets include ESA CCI products, other established EO climate records (NASA, EUMETSAT, Copernicus, NOAA), complementary satellite observations, and ground-based measurements. Together, they provide the foundation for subsequent quality assessments and comparative analyses (Task T2), supporting the refinement of resilience metrics and their application in large-scale case studies across diverse ecosystems.

1. ECOSYSTEM VARIABLES

1.1 EARTH-OBSERVATION DATA

1.1.1 LEAF AREA INDEX (LAI) and FRACTION OF ABSORBED PHOTOSYNTHETICALLY ACTIVE RADIATION (fAPAR)

The Leaf Area Index (LAI) is a dimensionless essential climate variable defined as one half of the total green leaf surface area per unit horizontal ground surface area, expressed in m^2 of leaf area per m^2 of ground area. LAI values generally range from 0 (bare ground) to about 10 in dense forest canopies. LAI is fundamental to characterizing land–atmosphere exchanges of energy, water, and carbon, influencing processes such as photosynthesis, transpiration, and rainfall interception (GCOS, 2024). The fraction of absorbed photosynthetically active radiation (fAPAR) is defined as the fraction of incoming solar radiation in the photosynthetically active radiation (PAR) spectral range (400–700 nm) that is absorbed by green vegetation. fAPAR is a dimensionless essential climate variable, ranging from 0 to 1, and is directly linked to plant photosynthetic capacity and gross primary production (ESA CCI,

2023a). Both LAI and fAPAR are recognized by the Global Climate Observing System as key vegetation state variables, critical for monitoring and modeling terrestrial ecosystem productivity, climate–vegetation interactions, and global climate change impacts (GCOS, 2024). A description of the main Earth observation datasets on LAI and fAPAR (Table 1) is provided below.

Table 1: Characteristics of datasets for LAI and fAPAR products

Dataset	Source (Instrument)	Spatial Resolution	Temporal Resolution	Coverage	Time Span	Remarks
CCI Vegetation LAI & fAPAR	ESA CCI Vegetation (SPOT4/5, VEGETATION1/2, PROB-V)	1 km	5-day composites	Transect/global sites	2000–2020	Essential Climate variable (ECV)
AVHRR LAI & fAPAR (v5)	NOAA/UMD AVHRR CDR (CDR AVHRR SR)	0.05° (~5 km)	Daily	Global land	1981–present	ECV
MODIS LAI & fAPAR (MCD15A2H)	NASA MODIS (Terra/Aqua)	500 m	8-day composite	Global land	2000–present	ECV
CGLS LAI & fAPAR	Copernicus (SPOT/VEG, PROBA-V,Sentinel 3-OLCI)	~1 km (1/112°) 300 m (recent)	10-day (decadal)	Global land	1999–present	
JRC-TIP LAI & fAPAR	JRC TIP (SeaWiFS, MERIS, SPOT-Vegetation, MODIS, Sentinel-3 OLCI, VIIRS)	~1 km (0.01°)	Monthly (aggregated)	Global land	1998–present	

CCI Vegetation LAI & fAPAR

The ESA Climate Change Initiative (CCI) Vegetation Parameters project has harmonized LAI and fAPAR datasets representing two Essential Climate Variables (ECVs) for carbon, water, and energy cycle monitoring. The Climate Research Data Package version 1.0 spans 2000–2020 and provides coverage along a north–south transect from Finland to South Africa, complemented by globally distributed validation sites (ESA CCI, 2024). Data is produced at 1 km spatial resolution with a 5-day temporal resolution, derived from symmetric 10-day composites. The retrieval method employs OptiSAIL radiative transfer model inversion applied to observations from SPOT-4/5 VEGETATION1/2 and PROBA-V sensors, ensuring temporal consistency across multiple missions. Output variables include LAI, fAPAR, their per-pixel uncertainties, and correlation coefficients, enabling robust uncertainty propagation in downstream analyses (Swinnen et al., 2023).

Strengths: Two decades of harmonized multi-mission observations provide a consistent record for assessing long-term vegetation dynamics and climate trends. The datasets offer high temporal granularity for detecting phenological events and short-term stress responses.

Accompanying uncertainty estimates and quality flags are included, supporting their assimilation into land-surface and ecosystem models.

Weaknesses: Spatial coverage is currently restricted, the research data package is not yet global, though a global extension is under development. Residual artifacts persist, including occasional striping, temporal noise, and outliers, particularly in evergreen broadleaf forest regions, where dense canopy saturation and sensor differences can be problematic. Cloud sensitivity can reduce effective temporal coverage in persistently overcast areas despite compositing. This is an archival product with no updates beyond 2020.

Access: The dataset is openly available via the ESA CCI Open Data Portal and the CEDA Archive in NetCDF format, with full documentation, processing chain descriptions, and validation reports (ESA CCI, 2024).

AVHRR CDR LAI and fAPAR (v5)

The NOAA Climate Data Record (CDR) of AVHRR LAI and fAPAR, Version 5 offers daily global estimates of LAI and fAPAR at 0.05° × 0.05° spatial resolution (≈ 5.5 km), derived from the AVHRR surface reflectance CDR (Vermote & NOAA CDR Program, 2019a; Google Earth Engine Developers, n.d.). The record spans 1981 to near-present (about 10 days before the current date, with NOAA-19 data quality declining post-2013) (NCEI, 2019; Google Earth Engine Developers, n.d.). The dataset is generated by applying an artificial neural network (ANN) model trained using MODIS LAI/fAPAR products and inputs from AVHRR surface reflectance and spectral indices, stratified by biome types. The approach utilizes the harmonized AVHRR surface reflectance CDR, which includes improved calibration, BRDF corrections, and alignment across multiple satellite sensors (Claverie et al., 2016; Vermote & NOAA CDR Program, 2019a).

Strengths: Very long-term record (1981–present) enables analysis of interannual and decadal trends in vegetation dynamics. Daily temporal resolution allows high-resolution phenology studies, drought detection, and model inputs. Consistent sensor calibration and harmonization across AVHRR platforms enhances temporal stability and inter-sensor continuity (Claverie et al., 2016; NCEI, 2019).

Weaknesses: Saturation in dense canopy areas (e.g., tropical forests), with LAI values plateau above ~4.5 m^2/m^2 and fAPAR above ~0.8, reducing sensitivity (Claverie et al., 2016). It has geolocation artifacts with slight inaccuracies in latitude (<0.002°) and longitude (<0.02°), and errors in the TIMEOFDAY variable (off by one day) (Google Earth Engine Developers, n.d.). There are sensor drift effects, namely quality degradation in later years due to NOAA-19 orbital drift compromises data reliability post-2013 (Google Earth Engine Developers, n.d.). It is a multi-instrument dataset, which complicates its use for resilience analysis (link to section in scientific requirements document).

Access: The dataset is openly hosted by NOAA NCEI. It is provided in NetCDF-4 format, compliant with CF and ACDD metadata standards, and accompanied by full algorithm documentation and data flow diagrams (NCEI, 2019; Vermote & NOAA CDR Program, 2019a).

MODIS LAI and fAPAR (MCD15A2H)

The MODIS MCD15A2H product provides global estimates of LAI and fPAR. This Version 6 dataset is derived from both the Terra (MOD15A2H) and Aqua (MYD15A2H) MODIS sensors, merged to produce an 8-day composite at 500 m spatial resolution from February 2000 to present (Myneni et al., 2015; Running et al., 2015). MCD15A2H is generated by inverting a three-dimensional radiative transfer model using MODIS surface reflectance (MOD09) as input. The algorithm employs a look-up table (LUT) approach (Knyazikhin et al., 1998a, 1998b), where canopy reflectances simulated for various LAI, fPAR, soil, and atmospheric conditions are compared to observed spectral bidirectional reflectance factors (BRFs) in the red and near-infrared bands. Retrievals are biome-specific, with vegetation classification provided by the MODIS land cover product (MCD12Q1). In cases where inversion fails, due to cloud contamination, poor angular sampling, or out-of-range BRFs, empirical back-up algorithms estimate LAI/fPAR from NDVI (Yang et al., 2006). The combined Terra–Aqua approach improves temporal coverage by leveraging the distinct overpass times of each platform.

Strengths: Moderate spatial resolution (500 m) with global coverage enables integration into ecosystem and climate models while preserving sub-kilometre heterogeneity. Frequent updates (8-day composites) capture seasonal dynamics and phenological transitions. Consistent multi-sensor record from two platforms increases data reliability and reduces gaps caused by cloud cover (Myneni et al., 2015). Extensive validation with field measurements through the CEOS Land Product Validation (LPV) program ensures quality control (Fang et al., 2019).

Weaknesses: Saturation in dense canopies (LAI > ~6 m^2/m^2) reduces sensitivity in tropical forests (Garrigues et al., 2008). Dependence on accurate land cover classification as misclassification can introduce systematic bias. Residual cloud and aerosol effects can degrade retrieval quality, especially in persistently cloudy regions.

Access: MCD15A2H is freely available from NASA's LP DAAC in HDF-EOS format, with per-pixel quality assurance (QA) flags and uncertainty indicators. The product can also be retrieved via Google Earth Engine.

CGLS LAI and fAPAR

The Copernicus Global Land Service (CGLS) LAI and fAPAR product provides global, 10-day composites at 1/112° spatial resolution from SPOT/VEG (1999-2014), and 300 m from the more recent PROBA-V (2014–2020) and Sentinel-3 OLCI (2020–present) optical instruments (Fuster et al., 2020; CGLS, 2023). The LAI/fAPAR retrievals employ the GEOV3 algorithm (Baret et al., 2013), which inverts the PROSAIL radiative transfer model using top-of-canopy reflectances in red, near-infrared, and shortwave infrared bands. The inversion is implemented via neural networks trained on simulated reflectances covering a wide range of canopy structures, soil backgrounds, and atmospheric conditions. Land cover information

guides biome-specific parameterization. The 10-day composites are derived using the Maximum Value Composite (MVC) method for fAPAR and a temporal smoothing/filtering approach for LAI, optimizing temporal consistency while retaining responsiveness to phenological changes (Verger et al., 2014).

Strengths: Daily acquisition with regular 10-day products balances temporal precision and noise reduction. Consistent multi-mission continuity ensured by harmonizing PROBA-V and Sentinel-3 OLCI data streams. Extensive validation through the CEOS LPV network, with documented accuracy meeting GCOS requirements (Fuster et al., 2020).

Weaknesses: Saturation in dense vegetation limits sensitivity beyond LAI ~6 m^2/m^2 and fAPAR ~0.8. Persistent cloud cover in tropical regions may lead to temporal gaps despite compositing. Sensor changes (PROBA-V to Sentinel-3) require cross-calibration, which can introduce subtle temporal inconsistencies (Mota et al., 2021).

Access: CGLS LAI and fAPAR products are freely available via the Copernicus Global Land Service portal (historical) and here, in NetCDF and GeoTIFF formats, with accompanying quality flags and uncertainty layers. Near-real-time (NRT) versions are also provided for operational monitoring, with an availability delay of 1–3 days.Leaf area index and fraction absorbed of photosynthetically active radiation 10-daily gridded data from 1981 to present

JRC-TIP LAI and fAPAR

The JRC-TIP (Joint Research Centre – Two-stream Inversion Package) dataset offers global estimates of LAI and fAPAR, reconstructed from broadband surface albedo observations through a physically based, data-driven retrieval methodology (Pinty et al., 2006). Products were originally generated under the ESA WACMOS-II project, using GlobAlbedo albedo inputs, and spanned the period of 1998–2011, with a spatial resolution of 1 km and daily retrievals, typically composited into seasonal to annual products (Disney et al., 2016). An early prototype series for fAPAR exists for 1998–2004 from SeaWiFS and MERIS sensors, developed as part of JRC's early fAPAR monitoring service (European Commission – Joint Research Centre, n.d.). LAI and fAPAR are retrieved by inverting a 1D two-stream radiative transfer model (JRC-TIP) against observed broadband VIS and NIR/SWIR albedo values. Unlike 3D canopy inversion approaches, this method avoids biome-specific structural assumptions, emphasizing consistency with Earth System Model radiation frameworks. Crucially, the inversion directly yields posterior uncertainty estimates, enhancing interpretability (Disney et al., 2016; European Commission – Joint Research Centre, n.d.). Although the initial JRC-TIP series was derived from multi-sensor fused albedo inputs like GlobAlbedo, more recent operational extensions primarily use MODIS albedo inputs, with ongoing transitions to VIIRS and Sentinel-3 OLCI for long-term continuity (Mota et al. 2021; Senguini et al. 2025).

Strengths: JRC-TIP exhibits high temporal stability, producing smoother phenological time series compared to MODIS due to the albedo assimilation and simplified 1D model structure (Disney et al., 2016). The method intrinsically provides uncertainty quantification via inversion posterior covariances, facilitating rigorous assimilation and error propagation (Disney et al., 2016). Structural simplicity, with absence of reliance on biome maps or canopy

clumping assumptions enhances global consistency. Cross-ECV analyses confirm high internal coherence between LAI and fAPAR changes in TIP, with the lowest rates of non-coherent variations globally (~5–10%) compared to products like MODIS or Copernicus Global Land Service (Mota et al., 2021).

Weaknesses: The 1D simplification may underestimate real canopy complexity, particularly in dense or clumped vegetation, potentially biasing LAI and fAPAR values downward (Disney et al., 2016). Relative to MODIS, JRC-TIP LAI values are systematically lower, ~60% of MODIS, with an offset of ~0.2 units, while fAPAR differences are smaller (~90–101% of MODIS with ~0.03 offset) (Disney et al., 2016). Coverage of the GlobalAlbedo-based product is restricted to 1998–2011, but continuity is maintained through MODIS-, VIIRS-, and Sentinel-3-based extensions, available up to present (2025) (European Commission – Joint Research Centre, n.d.; Seguini et al., 2025).

Access: The products were originally generated under the ESA GlobAlbedo project (1998-2011) and are distributed through the Joint Research Centre Data Catalogue. The fAPAR product is available in gridded formats (e.g., ASCII time series, NetCDF) along with pixel-level uncertainty estimates. A web interface supports extraction of time series for specific sites or geographic tiles (European Commission – Joint Research Centre, n.d.; European Space Agency, 2013). Updated JRC-TIP LAI/fAPAR datasets extending to 2025, based on MODIS, VIIRS, and Sentinel-3 OLCI inputs, are accessible via de JRC FAPAR portal and the JRC Data Catalogue.

1.1.2 VEGETATION INDICES (NDVI/EVI)

A vegetation index is a dimensionless, radiometric indicator calculated using reflectance values in specific spectral bands, most commonly the red and near-infrared (NIR) regions, designed to highlight vegetation biophysical properties (Myneni et al. 1995). Descriptions of the main datasets on vegetation indexes, namely the Normalized Difference Vegetation Index (NDVI) and the Enhanced Vegetation Index (EVI) (Table 2) are provided below.

Table 2: Characteristics of Dataset for Vegetation Indices products

Dataset	Source (Instrument)	Spatial Resolution	Temporal Resolution	Coverage	Time Span
MODIS NDVI/EVI	NASA MODIS (Terra, e.g. MOD13A1)	250 m 500 m 1 km	16-day composite	Global land	2000–present
AVHRR NDVI (v5)	NOAA/UMD AVHRR CDR	0.05° (~5 km)	Daily	Global land	1981–present
Sentinel-2 NDVI	ESA Sentinel-2 (MSI)	10 m (NDVI), 20 m (EVI)	~5-day revisit (multi-sat)	Global land	2017–present
Landsat NDVI	USGS Landsat 5,7,8/9	30 m	16-day (per satellite)	Global land	1984–present

MODIS NDVI/EVI

The MODIS Vegetation Indices (VI) products, including the NDVI and EVI, are generated from MODIS instruments aboard NASA's Terra (MOD13) and Aqua (MYD13) satellites. The most widely used versions are the MOD13Q1/MYD13Q1 16-day composites at 250 m spatial resolution, MOD13A1/MYD13A1 16-day composites at 500 m, and MOD13A2/MYD13A2 16-day composites at 1 km, as well as MOD13C1/MYD13C1 global 0.05° gridded products (Didan, 2015; Didan et al., 2015). The record spans February 2000–present for Terra and July 2002–present for Aqua. MODIS VI products are computed from atmospherically corrected surface reflectance (MOD09/MYD09), using a compositing approach that selects the "best" pixel within a 16-day period based on maximum NDVI and additional quality metrics (Huete et al., 2002).

Strengths: Long-term, consistent multi-resolution record supporting vegetation monitoring from local to global scales. EVI reduces atmospheric and background noise and is less prone to saturation in dense vegetation compared to NDVI (Huete et al., 2002). Quality assurance layers allow filtering for cloud, aerosol, and view geometry effects.

Weaknesses: NDVI saturates in dense canopies (LAI > ~3), limiting discrimination in tropical forests (Myneni et al., 1995). EVI can be sensitive to residual atmospheric correction errors in the blue band. Compositing may smooth short-term dynamics, potentially masking rapid phenological events.

Access: MODIS VI products, including NDVI and EVI, are freely available from multiple platforms. A detailed description and overview are available via NASA's official MODIS Vegetation Index portal. The datasets themselves can be downloaded in HDF-EOS format from NASA´s LP DAAC (MOD13Q1 v6.1, MOD13A1 v6.1, MOD13A2 v6.1, MOD13A3 v6.1) and through Google Earth Engine (MOD13Q1 v6.1, MOD13A1 v6.1, MOD13A2 v6.1, MOD13A3 v6.1) with global coverage and full QA documentation.

AVHRR NDVI

The Advanced Very High-Resolution Radiometer (AVHRR) NDVI Climate Data Record (CDR) provides a harmonized, long-term measure of global vegetation greenness derived from the AVHRR sensors aboard NOAA's polar-orbiting satellites. The current NOAA CDR Version 5 spans July 1981 to present, offering 0.05° (~5.6 km) spatial resolution and daily temporal coverage, with global extent (Vermote & NOAA CDR Program, 2019b). NDVI is computed using atmospherically corrected surface reflectances from AVHRR channels 2 (near-infrared, 0.725–1.10 µm) and 1 (red, 0.58–0.68 µm) (Kidwell, 1998). The CDR is derived from the AVHRR Surface Reflectance CDR, which includes calibration harmonization across multiple AVHRR sensors, cloud screening, Rayleigh/aerosol correction, and bidirectional reflectance distribution function (BRDF) adjustment (Vermote & NOAA CDR Program, 2019b). Daily NDVI values are generated and can be composited into 7-day, 10-day, or monthly means by users.

Strengths: Longest continuous global NDVI record (1981–present) suitable for multi-decadal trend analysis in vegetation productivity and phenology (Pinzon & Tucker, 2014). Daily

temporal resolution enables fine-scale phenological and drought monitoring when composited appropriately. Cross-sensor calibration and atmospheric correction reduce artefacts from sensor changes and orbital drift.

Weaknesses: Broad spectral bands and lower radiometric sensitivity compared to modern sensors can reduce discrimination in sparse vegetation and mixed pixels. Geometric registration errors in early years and residual BRDF effects can affect time series consistency (Tucker et al., 2005). NDVI saturates in high-biomass regions (e.g., tropical forests), limiting sensitivity at LAI > ~3 (Myneni et al., 1995).

Access: The AVHRR NDVI CDR is freely available from NOAA's National Centers for Environmental Information (NCEI) in NetCDF-4 format, compliant with CF and ACDD metadata conventions. It is also accessible via Google Earth Engine (NOAA/CDR/AVHRR/NDVI/V5), with full quality assurance layers and documentation. It is a multi-instrument dataset, which complicates its use for resilience analysis (link to section in scientific requirements document).

Sentinel-2 NDVI/EVI

The Sentinel-2 NDVI and EVI datasets are derived from multispectral observations collected by the Sentinel-2A (launched June 2015) and Sentinel-2B (launched March 2017) satellites, part of the Copernicus Programme operated by ESA. Each satellite carries a MultiSpectral Instrument (MSI), providing 13 spectral bands from visible to shortwave infrared, with spatial resolutions of 10 m (visible, NIR), 20 m (red edge, SWIR), and 60 m (atmospheric bands) (Drusch et al., 2012). The constellation achieves a 5-day revisit at the equator (higher at mid-latitudes). NDVI is calculated from atmospherically corrected bottom-of-atmosphere reflectances in the red (Band 4, 665 nm) and near-infrared (Band 8, 842 nm) bands. EVI uses red, NIR, and blue (Band 2, 490 nm) reflectances to minimize soil and atmospheric effects (Huete et al., 2002). Atmospheric correction is typically performed with Sen2Cor to obtain Level-2A surface reflectance products (Main-Knorn et al., 2017). NDVI/EVI layers are either generated on-the-fly in platforms like Google Earth Engine or pre-computed in third-party products (e.g., Copernicus Global Land Service).

Strengths: Very high spatial resolution (10 m) allows fine-scale vegetation monitoring, agricultural mapping, and ecosystem health assessment. High revisit frequency from twin satellites captures rapid vegetation changes and short-term disturbances. Rich spectral coverage includes red-edge bands useful for vegetation structure analysis and improved LAI retrievals.

Weaknesses: Limited temporal record (since 2015/2017) compared to MODIS or AVHRR, restricting long-term trend studies. Cloud contamination and shadows can limit usable observations, particularly in tropical and temperate wet climates. EVI sensitivity to blue band noise under hazy conditions if atmospheric correction is imperfect.

Access: Sentinel-2 Level-2A surface reflectance data (atmospherically corrected) are openly available via Copernicus Data Space Ecosystem and Google Earth Engine. NDVI/EVI can be

computed directly from reflectances or retrieved as ready-to-use vegetation index products in various analysis platforms.

Landsat NDVI

The Landsat NDVI dataset is derived from surface reflectance observations collected by the Landsat series of satellites, Landsat 4–5 Thematic Mapper (TM), Landsat 7 Enhanced Thematic Mapper Plus (ETM+), and Landsat 8–9 Operational Land Imager (OLI), managed jointly by NASA and the U.S. Geological Survey (USGS). Landsat provides a 30 m spatial resolution in the visible and near-infrared (NIR) bands, with a 16-day revisit cycle per satellite; the combined Landsat 7 and Landsat 8 constellation achieves an 8-day revisit globally (Roy et al., 2014; Wulder et al., 2022). NDVI is computed from atmospherically corrected bottom-of-atmosphere reflectances in the red and near-infrared bands. Atmospheric correction is performed using the LEDAPS algorithm for TM/ETM+ and the LaSRC algorithm for OLI, producing Level-2 surface reflectance products (Vermote et al., 2016; USGS, 2019). NDVI can be computed by users or accessed via pre-computed products in Google Earth Engine (e.g., LANDSAT/LT05/C02/T1_L2, LANDSAT/LE07/C02/T1_L2, LANDSAT/LC08/C02/T1_L2).

Strengths: High spatial resolution (30 m) enables detailed mapping of vegetation condition, agricultural fields, and landscape heterogeneity (Wulder et al., 2022). Continuous record since 1984 allows multi-decadal change detection and time-series analysis when harmonized across sensors (Roy et al., 2014). Well-documented radiometric calibration and atmospheric correction improve temporal consistency.

Weaknesses: 16-day revisit cycle limits temporal density and cloud cover can further reduce usable observations, especially in humid climates (Zhu & Woodcock, 2014). Sensor differences (e.g., spectral response changes from TM/ETM+ to OLI) require cross-calibration for long-term consistency. Saturation in high-biomass vegetation reduces sensitivity in dense tropical forests (Myneni et al., 1995).

Access: Landsat Level-2 surface reflectance products are freely available through multiple official portals: USGS EarthExplorer (all Landsat missions since 1972; see also here), and Google Earth Engine. Vegetation indices such as NDVI can be computed directly from surface reflectance bands or accessed as ready-to-use time-series datasets in cloud platforms such as Google Earth Engine.

1.1.3 VEGETATION OPTICAL DEPTH (VOD)

Vegetation Optical Depth (VOD) is a model-derived vegetation metric that quantifies the attenuation of natural microwave radiation by vegetation. VOD quantifies canopy attenuation of microwave radiation and correlates with vegetation water content, biomass, and phenology. VOD becomes increasingly sensitive to the canopy's uppermost layers as the

sensing wavelength shortens (Konings et al., 2019). Accordingly, spatial and temporal patterns retrieved at higher frequencies (C, X, and Ku-band) tend to mirror upper-canopy dynamics more closely (Schmidt et al., 2023). By contrast, lower frequencies (L-band) better reflect total above-ground biomass (AGB), including woody components such as branches and trunks (Schmidt et al., 2023). As a proxy for canopy water content and biomass, VOD provides critical insight into the Earth's terrestrial ecosystems (Moesinger et al. 2020). Unlike optical vegetation indices, VOD is independent of cloud cover and solar illumination and can penetrate vegetation layers to varying degrees, depending on the microwave frequency used. Several global datasets now exist (Table 3), varying in spatial and temporal resolution, frequency sensitivity, and methodological approach.

Table 3: Characteristics of datasets for Vegetation Optical Depth (VOC) products

Dataset	Source (Sensors)	Spatial Resolution	Temporal Resolution	Coverage	Time Span
VODCA C-band	Microwave sensors (SSM/I, AMSR-E, WindSat…)	0.25°	Daily	Global land	2002–2018
VODCA X-band	Same as above	0.25°	Daily	Global land	1997–2024
VODCA Ku-band	Same as above	0.25°	Daily	Global land	1987–2024
VODCA CXKu (merged)	Combined X+Ku from VODCA v2 (passive)	0.25°	Daily	Global land	1987–2024
VODCA L-band	SMOS/SMAP (L-band radiometers)	0.25°	10-day composite	Global land	2010–2023
SVODI	Standardized VOD index (C+X+Ku)	0.25°	Daily	Global land	1987–2019
SMOS-IC VOD	SMOS-IC (L-band, Land)	0.25° (25 km)	Daily	Global land	2010–present
GLAB-VOD	SMAP-IB	0.25°	18-day composite	Global land	2002-2020

VODCA (C-, X-, Ku-, CXKu-, and L- bands)

The VOD Climate Archive (VODCA) provides long-term, harmonized global records of vegetation optical depth derived from passive microwave radiometers using the the Land Parameter Retrieval Model (LPRM) (Owe et al., 2008; Moesinger et al., 2020; Zotta et al., 2024). All products are gridded at 0.25° spatial resolution and offered at daily temporal resolution, with only nighttime overpasses used to minimize thermal artifacts. **Multi-instrument products:** Retrievals from multiple sensors (SSM/I, TMI, AMSR-E, AMSR2, WindSat, GMI) are harmonized via cumulative distribution function (CDF) matching to AMSR-E as a reference, with overlapping records merged into continuous climate data records. The VODCA C-band (~6.9 GHz) spans 2002–2024, integrating AMSR-E, AMSR2, and WindSat observations. The VODCA X-band (~10.7 GHz) extends further, 1997–2024, exploiting TMI, AMSR-E/2, and WindSat. The VODCA Ku-band (~19 GHz) provides the longest

record, 1987–2024, based on SSM/I, TMI, AMSR-E/2, and WindSat, and is especially responsive to leaf water content, supporting assessments of short-term vegetation dynamics. The most recent VODCA v2 CXKu composite integrates C, X, and Ku bands from 1987–2024 and data from two additional sensors, SSMI F17 and GMI, reducing retrieval noise while maximizing temporal coverage. Complementary L-band VOD records (2010–2023, 10-day, ~25 km), based on SMOS and SMAP data, target woody biomass but at lower temporal frequency (Zotta et al., 2024). **Single-sensor products:** VOD data from multiple individual sensors (e.g., AMSR2, AMSR-E, TMI), in the C-, X- and Ku-band frequencies, will be improved based on the method of Zotta et al., 2025, and processed within SIRENE.

Strengths: The VODCA datasets provide multi-decadal, all-weather, day–night coverage, independent of solar illumination and largely unaffected by cloud contamination, enabling robust monitoring of vegetation dynamics, biomass, and drought responses. Multi-sensor harmonization and frequency-specific retrievals allow complementary insights into different canopy layers, while quality flags ensure transparency. Availability of both multi-and single-sensor products for SIRENE enable resilience analysis in regions where unreasonable signal-to-noise ratios hinder the use of multi-instrument datasets.

Weaknesses: The coarse spatial resolution (0.25°) limits local-scale applications. Frequency-dependent sensitivities mean that C- and X-band emphasize foliage, whereas deeper woody biomass is underrepresented (better captured by L-band). Residual inter-sensor artifacts and retrieval uncertainties persist in complex terrain, frozen ground, and regions with radio-frequency interference (RFI). Multi-frequency merging in CXKu, while reducing noise, may give rise to false signals of resilience.

Access: All multi-instrument VODCA products are openly available in NetCDF-4 format under a CC BY 4.0 license via Zenodo and the TU Wien Research Data Portal, with accompanying sensor masks and quality-control layers (Moesinger et al., 2020; Zotta et al., 2024).

SVODI (Standardized VOD Index)

The Standardized Vegetation Optical Depth Index (SVODI) is a harmonized, long-term global index that quantifies deviations in vegetation conditions using microwave-derived Vegetation Optical Depth (VOD). It spans 1987–2019, offers daily temporal resolution, and is gridded at 0.25° × 0.25° spatial resolution (Moesinger et al., 2022a, 2022b). SVODI is computed by merging VOD estimates from multiple passive microwave sensors and frequencies, namely C-, X-, and Ku-band observations, from SSM/I, TMI, AMSR-E, WindSat, and AMSR2. The merging employs a probabilistic statistical framework, specifically standardizing each VOD time series and combining them to create a unified anomaly index. This method maintains consistency across heterogeneous sensor records and addresses heteroscedasticity, ensuring that even with varying data availability over time, SVODI reliably represents vegetation condition deviations (Moesinger et al., 2022a).

Strengths: Extended temporal coverage from 1987 to 2019 delivers robust climate-scale monitoring of vegetation anomalies. All-weather, daily data afford consistent temporal

sampling, regardless of solar illumination or cloud cover. By integrating multiple frequency bands, SVODI is sensitive to anomalies in different canopy layers, improving catchment of drought, greenness shifts, and vegetation stress responses. The index's standardization enables direct comparison with optical indices (e.g., VHI) and drought indicators (e.g., scPDSI), as shown through strong temporal correlations (Moesinger et al., 2022a).

Weaknesses: Coarse spatial resolution (0.25°) limits utility for local or field-scale ecological applications. Potential artifacts may persist in areas with complex topography, snow/ice cover, or radio-frequency interference (RFI). As an anomaly index, SVODI does not convey absolute biomass, but it reflects relative deviations from mean conditions. The data are available only until 2019.

Access: SVODI is openly available via Zenodo, licensed under CC BY 4.0, in daily NetCDF files covering 1987–2019, with embedded sensor-contribution flags for quality tracing and provenance (Moesinger et al., 2022b).

SMOS-IC L-band VOD

The SMOS-IC (INRAE–CESBIO) L-band VOD product is retrieved from ESA's SMOS multi-angular L-band (~1.4 GHz) brightness temperatures (BTs) measured by MIRAS. It is delivered on the EASE-Grid 2.0 at 0.25° (~25 km) spatial resolution with daily temporal resolution, globally. The record began in 2010 (start of SMOS operations). The widely used public archives provide 2010–present coverage for v2, with ongoing updates thereafter (Wigneron et al., 2021; INRAE, 2020/2025). SMOS-IC inverts the L-MEB τ–ω radiative transfer model for soil moisture and L-VOD using SMOS BTs (incidence angles ≈20°–55°), minimizing the use of external ancillary data (e.g., ECMWF skin temperature) to reduce propagation of non-microwave uncertainties (Fernandez-Moran et al., 2017). Version 2 introduces a temporal constraint: the a-priori VOD at day t is initialized from VOD retrieved during the preceding 10 days, stabilizing estimates while preserving dynamics. The per-pixel standard error layers and quality flags (Scene_Flags, BT-RMSE) support rigorous filtering (Wigneron et al., 2021; INRAE, 2020/2025).

Strengths: It has all-weather, day–night sensitivity independent of solar illumination/clouds. It enables deep canopy penetration at L-band, enhancing sensitivity to woody components and above-ground biomass (AGB). Simplified, microwave-centric retrieval reduces dependence on optical/land-cover auxiliaries. Demonstrated skill for above-ground biomass (AGB) and carbon-stock change assessments (Mialon et al., 2020; Wigneron et al., 2021).

Weaknesses: Coarse spatial resolution (25 km) limits field-scale applications. It has radio-frequency interference (RFI), complex topography, frozen surfaces, or open-water contamination can bias retrievals, hence recommended filtering using Scene Flags and TB-RMSE ≤ 6 K. The temporal coverage begins in 2010, shorter than multi-decadal higher-frequency VOD archives (INRAE, 2020/2025; Wigneron et al., 2021).

Access: SMOS-IC L-VOD (v2) is distributed as NetCDF-4, daily global grids on EASE2 25 km, via CATDS/ESA and INRAE Bordeaux portals and here (data from 2010–present is available), with

guidance for obtaining the most recent filtered releases (INRAE, 2020/2025; Wigneron et al., 2021).

GLAB-VOD

GLAB-VOD (Global L-band Equivalent AI-Based Vegetation Optical Depth) provides a global record of VOD spanning the years 2002–2020 (with a ~9 month gap from October 2011 to July 2012 due to sensor transition) at 25 km on the EASE-2 grid, with 18-day temporal resolution (VOD). A companion GLAB-TB product provides daily 25 km brightness temperatures (TB). The record integrates both true L-band observations (SMOS TB: 2010-2020; SMAP-IB VOD: 2015-present) and L-band equivalent reconstructions from AMSR-E (2002-2011) and AMSR-2 (2012-2020), mapped to the SMAP-IB distribution using a multi-stage neural network architecture (Skulovich et al. 2024). SMOS-like TB are derived from AMSR TB via transfer learning, which are then combined with CASM soil moisture (3 day, 25 km) to predict SMAP-IB VOD. The workflow includes seasonal cycle decomposition and an ensemble of seven neural networks, providing mean VOD and ensemble-based uncertainty (Skulovich et al., 2024; Skulovich & Gentine, 2023; Li et al., 2022).

Strengths: Temporal consistency across sensors, supports uncertainty quantification, and demonstrates high spatial correlations with biomass (R≈0.92) and canopy height (R≈0.93), matching or exceeding SMAP-IB performance (Skulovich et al., 2024).

Weaknesses: Smoothing of high-frequency variability relative to SMAP-IB (e.g., muted high-latitude 2019 peak). The RFI and frozen-soil effects reduce data density regionally despite SMOS filtering. The 25 km/18-day resolution limits local or event-scale analyses. Users should exploit provided uncertainty fields and consider biome-/latitude-specific behavior (Skulovich et al., 2024).

Access: GLAB-VOD dataset along with the companion GLAB-T, is openly accessible under a CC BY 4.0 license via Zenodo (Skulovich et al., 2023, 2024).

TMI X-band VOD

The TMI-X-band VOD product derives vegetation optical depth (VOD) from the Tropical Rainfall Measuring Mission (TRMM) Microwave Imager (TMI), a joint mission of NASA and JAXA. X-band VOD is retrieved from observations in the X-band (~10.7 GHz). These retrievals are generated using the Land Parameter Retrieval Model (LPRM). The dataset spans December 1997 to April 2015 at a spatial resolution of ~25km from 40S to 40N.

Strengths: Long observation time for a VOD product (1997-2015), daily revisit time. It has all-weather, day–night sensitivity independent of solar illumination/clouds.

Weaknesses: Coarse spatial resolution (25 km) limits field-scale applications and is restricted to 40S to 40N. Relatively shallow penetration of canopy, and might thus be saturation-prone.

Radio-frequency interference (RFI), complex topography, frozen surfaces, or open-water contamination can bias retrieval. Only available until 2015. Potentially old retrieval algorithm optimized for the retrieval of soil moisture instead of VOD.

Access: The information is available at NASA EarthData and open access data also via NASA.

AMSR-E X- & C-band VOD

AMSR-E X- & C-band VOD is retrieved from the Advanced Microwave Scanning Radiometer–Earth Observing System (AMSR-E) aboard NASA's Aqua satellite, covering the period June 2002 to October 2011—the operational lifetime of AMSR-E. It leverages multiple microwave frequencies, including X-band (~10.7 GHz) and C-band (~6.9 GHz). VOD is retrieved via the Land Parameter Retrieval Model (LPRM) that simultaneously retrieves surface soil moisture, vegetation optical depth (VOD), and land surface (skin) temperature using the τ-ω radiative transfer model. It is available separately for the night-time and daytime overpasses.

Strengths: C-band VOD can potentially penetrate deeper than X-band. Having VOD from two different frequencies available allows their comparison. Minimal dependency on external data beyond brightness temperatures, simplifying data processing pipelines. Separate night-time overpass retrieval should provide enhanced VOD due to reduced influence of temperature anomalies.

Weaknesses: Compared to e.g. L-band VOD, both X- but also C-VOD can rather penetrate the canopy only and might saturate in high biomass areas. The daily ~25 km grid smoothes fine-scale variability, reducing responsiveness to rapid vegetation dynamics. Radio-frequency interference (RFI), complex topography, frozen surfaces, or open-water contamination can bias retrieval. Potentially old retrieval algorithm optimized for the retrieval of soil moisture instead of VOD.

Access: Information available at
https://disc.gsfc.nasa.gov/datasets/LPRM_AMSRE_D_SOILM3_002/summary and data at
https://hydro1.gesdisc.eosdis.nasa.gov/data/WAOB/LPRM_TMI_NT_SOILM3.001/

AMSR2 C1- & C2-band VOD

AMSR2 C1- and C2-band VOD represents vegetation optical depth (VOD) retrievals derived from the Advanced Microwave Scanning Radiometer 2 (AMSR2), operating on JAXA's GCOM-W1 satellite launched in May 2012 (successor to AMSR-E). Data for ascending and descending orbits are available on a daily basis. These products exploit dual C-band channels—C1 (~6.9 GHz) and C2 (~7.3 GHz)—to capture vegetation water content related to canopy structure and biomass. VOD retrievals are generated via the Land Parameter

Retrieval Model (LPRM), which solves for soil moisture and vegetation optical depth (as well as surface effective temperature) using the τ-ω radiative transfer model applied to dual-polarized brightness temperatures. The AMSR2 design includes improved calibration and RFI mitigation (e.g., the added 7.3 GHz channel) to enhance data quality over its predecessor.

Strengths: Enhanced sensitivity to vegetation structure and water content, particularly appropriate for moderate canopy densities. Improved data fidelity through enhanced calibration and RFI avoidance with the 7.3 GHz channel, which helps reduce contamination in retrievals. Minimal external data dependency: LPRM relies primarily on its own brightness temperature inputs rather than extensive ancillary datasets.

Weaknesses: Weaker deep canopy penetration and reduced sensitivity compared to lower-frequency bands like L-band, and especially in dense tropical forests saturation could be an issue. Spatial resolution of ~25km hinders field-scale applications. Complex topography, frozen surfaces, or open-water contamination can bias retrieval. Potentially old retrieval algorithm optimized for the retrieval of soil moisture instead of VOD.

Access: Information available at https://cmr.earthdata.nasa.gov/search/concepts/C1235316198-GES_DISC.html and data:

- Download descending (nighttime): https://hydro1.gesdisc.eosdis.nasa.gov/data/WAOB/LPRM_AMSR2_D_SOILM3.001/
- Download ascending (daytime): https://hydro1.gesdisc.eosdis.nasa.gov/data/WAOB/LPRM_AMSR2_A_SOILM3.001/2023/08/

SMOS L-band VOD (CATDS)

The SMOS L-band VOD (CATDS) is a global soil moisture product derived from SMOS satellite data provided by ESA. It aggregates daily soil moisture maps into 3-day, 10-day, and monthly composites. Ascending and descending orbit data are processed separately, ensuring orbit-specific continuity and consistency. The record spans January 2010–present, with a reprocessed segment (RE07, 2010–May 2021) and a continuous operational stream (OPER, June 2021–present) using the same algorithms to ensure temporal consistency. The data is distributed on the global EASE-Grid 2.0 (~30-50km) in NetCDF-3 format. Naming conventions encode product type, aggregation period (3, D, M), processing version (RE07 or OPER), and orbit (A or D).

Strengths: The product provides long-term temporal continuity across reprocessed and operational phases, enabling climate-scale studies. Multiple aggregation windows (3-day, 10-day, monthly) allow flexible analysis from short-term to seasonal scales. Orbit-specific processing preserves subtle differences between ascending/descending passes, which can

be useful for bias detection or hydrological cycle investigations. Usually prefer night-time orbits.

Weaknesses: The monthly data's aggregation might smooth high-frequency variability, limiting sensitivity to short-lived events (e.g., flash droughts, irrigation pulses). The extremely coarse grid constrains local-scale applications. As with all SMOS products, retrievals may be impacted regionally by radio-frequency interference (RFI) and frozen-soil conditions. The retrieval algorithm is optimized for the retrieval of soil moisture, not VOD.

Access: Information available at https://sextant.ifremer.fr/record/b57e0d3d-e6e4-4615-b2ba-6feb7166e0e6/ and data can be downloaded as open access under CC BY license via CATDS/IFREMER servers at https://data.catds.fr/cpdc/Land_products/GRIDDED/L3SM/RE07/MIR_CLF3MA/

1.1.4 SUN-INDUCED CHLOROPHYLL FLUORESCENCE (SIF), ABOVE-GROUND BIOMASS AND LAND COVER

SIF is a faint red to far-red emission (≈650–850 nm) re-emitted by chlorophyll molecules during photosynthesis and serves as a direct, mechanistic proxy for gross primary production (GPP). (European Space Agency [ESA], 2014; Celesti, 2020). The above-ground biomass (AGB) describes the dry mass of the above-ground woody parts of trees expressed in Mg ha^{-1} (ESA, n.d.-a). Land cover refers to the physical material present at Earth's surface (e.g., trees, grass, water, bare ground, built-up surfaces), as defined and produced in ESA's Land Cover CCI (ESA, n.d.-b). A description of the mentioned variables is provided in Table 4.

Table 4 Characteristics of Datasets for SIF, AGB and Land-cover products

Ecosystem variables	Dataset	Spatial resolution	Temporal resolution	Coverage	Time Span	Remarks
SIF	GOME-2 SIF	40x80 km (before 2013) /40x40 km	Daily	Global	2007 - 2023	
SIF	CSIF	0.50°	4-daily	Global	2000-2020	
Above-ground Biomass	CCI Biomass	100 m	Yearly	Global	2007, 2010, 2015-2022	
Land Cover	CCI Landcover	300 m	Yearly	Global	1992 - 2022	
Radar backscatter	LHScat	0.25°	Monthly	Global	1992-2022+	

GOME-2 SIF

The Global Ozone Monitoring Experiment-2 (GOME-2) Sun-Induced Fluorescence (SIF) datasets provide long-term, global estimates of photosynthetic activity derived from hyperspectral radiance measurements in the oxygen A-band. GOME-2 instruments onboard EUMETSAT's MetOp-A (2007–2022), MetOp-B (2012–2023), and MetOp-C (2018–present) polar-orbiting satellites operate in a sun-synchronous morning orbit (~09:30 LT). Current SIF products typically span 2007–present, with 0.5° × 0.5° spatial resolution (native footprint ~40 × 80 km²) and daily global coverage aggregated to 8-day or monthly composites (Joiner et al., 2013; Köhler et al., 2015). SIF retrieval exploits the in-filling of Fraunhofer lines in high-resolution spectra measured in the 734–758 nm region, dominated by O_2 absorption. The most widely used processing chains (e.g., NASA GSFC and GOME-2 FAPAR/SIF algorithms) employ Principal Component Analysis (PCA) to model and remove reflected solar radiance, isolating the fluorescence signal (Joiner et al., 2013). Calibration across the three GOME-2 sensors ensures temporal consistency, with cross-normalization during overlap periods (Köhler et al., 2015).

Strengths: Direct proxy for photosynthetic activity, less affected by confounding structural and background effects compared to greenness indices (e.g., NDVI). Global, long-term record (2007–present) enabling climate-scale analyses of vegetation productivity. Morning overpass time reduces the influence of midday cloud build-up and yields stable illumination conditions. The coarse footprint allows for consistent spatial coverage across heterogeneous landscapes.

Weaknesses: Coarse native resolution (tens of km) limits fine-scale ecosystem studies; aggregation to 0.5° further smooths spatial detail. Cloud contamination and atmospheric scattering can bias retrievals, particularly in persistently cloudy or high-aerosol regions. Retrieval noise increases over dark targets (e.g., dense forests, low sun angles), requiring multi-day averaging for robust signals.

Access: GOME-2 SIF datasets are openly available. Specifically, TEMIS (EUMETSAT official archive) for monthly, gridded Level-3 products (e.g., climate/vegetation studies), coverage mainly GOME-2B (2012-2023); NASA ORNL DAAC for daily, orbital L2 products (detailed temporal studies, e.g. flux tower comparisons), coverages: GOME-2A (MetOp-A: 2007-2018), GOME-2B (MetOp-B: 2013-2021), GOME-2C (MetOp-C: 2019-present) and NASA GES DISC (2002-2018) Level-3 harmonized datasets that combine multiple sensors (e.g., SCIAMACHY+GOME-2). Temporally consistent SIF (TCSIF), a special GOME-2A dataset with sensor degradation corrected, ensuring long-term consistency, coverage 2007-2021.

CSIF

CSIF (Contiguous Solar-Induced Fluorescence) provides two global SIF products generated with a neural network trained on MODIS surface reflectances and OCO-2 SIF: (i) clear-sky instantaneous CSIF and (ii) all-sky daily CSIF. Both are delivered at 0.05° (~5 km) spatial resolution and 4-day temporal resolution for the MODIS era: 2000–2017 (original release), with extensions to 2020 via updated MODIS/BESS inputs (Zhang et al., 2018). The authors

report strong agreement with OCO-2 and GOME-2 SIF and a global increasing trend in daily CSIF (~0.39 % yr^{-1}) (Zhang et al., 2018). OCO-2 SIF (757/771 nm) is aggregated to 0.05° and used with MODIS reflectances and cos(SZA) to train the NN under clear-sky conditions; predictions yield CSIF_clear-inst. Daily CSIF is obtained by scaling with daily PAR (BESS) and a clear-to-daily correction; an all-sky daily version incorporates cloud effects via BESS radiation. (Sun et al., 2018; Zhang et al., 2018).

Strengths: Spatially contiguous SIF at 5 km/4-day globally across two decades. High coherence with OCO-2/GOME-2 seasonality and interannual variability. Useful for GPP inference and drought monitoring via the OCO-2/CSIF ratio as a stress indicator (Zhang et al., 2018).

Weaknesses: Model-based reconstruction (NN) may bias unusual atmospheric/biome conditions. All-sky daily CSIF shows modest underestimation versus satellite daily SIF. Dependence on MODIS-era inputs and 4-day averaging can smooth high-frequency dynamics. Independent assessments caution that reconstructed SIF products differ in temporal fidelity and uncertainty (Zhang et al., 2018; Shekhar et al., 2022).

Access: Public releases are hosted on: i) Figshare (global grids at 0.05° and 0.5° resolution (Zhang et al. 2018 - DOI: 10.6084/m9.figshare.6387494.v2), including updates through 2020; ii) TPDC (National Tibetan Plateau Data Center), with high resolution (0.05°/ 4-day) distributions (DOI: 10.11888/Ecolo.tpdc.271751) and OSF repository, an original release (DOI: 10.17605/OSF.IO/8XQY6; updated through 2022), with files organised by clear-sky instantaneous (CSIF_clear-inst) and all-sky daily (CSIF_all-daily) products. All files are distributed in NetCDF format (time series of global gridded data). Supporting code for dataset generation and analysis is openly available on GitHub (linked from the dataset landing pages).

ESA CCI Biomass

The ESA Climate Change Initiative (CCI) Biomass product provides global maps of forest above-ground biomass (AGB) and per-pixel uncertainty. The latest release (v6.0) delivers annual epochs for 2007, 2010, and 2015–2022, with full-resolution maps at 1 ha (≈100 m) and aggregated layers at 1, 10, 25, and 50 km (Santoro & Cartus, 2025; ESA CCI Biomass Team, 2023). AGB is estimated by fusing C- and L-band SAR backscatter (Envisat ASAR, Sentinel-1, ALOS-1/2 PALSAR) and calibrating with spaceborne lidar (ICESat-2; formerly ICESat/GEDI where available). Retrieval follows the BIOMASAR family of algorithms: (i) derive growing stock volume (GSV) from multi-temporal SAR; (ii) convert to AGB using biome-specific expansion/conversion factors; and (iii) apply a cost function that enforces temporal consistency across years, limiting biases between early (2007–2010) and later (2015+) maps (Santoro & Cartus, 2025; Santoro et al., 2021; ESA CCI, n.d-a). The official v5 fact sheet documents the 100 m grid (1 ha pixel) and warns that AGB change is delivered with standard-deviation and quality-flag layers rather than a single “difference” raster (Santoro, 2024).

Strengths: High-resolution (100 m) global maps across multiple epochs enable decadal and inter-annual biomass-change assessments. The per-pixel standard deviation and quality flags support uncertainty propagation and multi-sensor SAR plus ICESat-2 calibration improves robustness across biomes. The v6 extends the record to 2007–2022, providing consistent inputs for REDD+, carbon-budgeting, and model benchmarking (Santoro & Cartus, 2025; ESA CCI, 2025a; Santoro et al., 2021).

Weaknesses: Radar saturation persists in very dense tropical forests, reducing sensitivity at high AGB. The cross-sensor harmonization (ASAR/S-1/ALOS) and differing data availability mean that 2010 vs. 2015+ comparisons require care. The maps are not forest-masked and pixel values represent the full 1-ha area and AGB-change analyses must use the provided quality flags and SD layers to avoid spurious trends (Santoro, 2024; Santoro & Cartus, 2025).

Access: Open and citable via the ESA CCI Open Data Portal in GeoTIFF/NetCDF formats, with DOI-linked downloads including aggregated 1–50 km products and change/uncertainty layers; subsets archived at CEDA- Version 5 (2024- Global AGB for select years 2010-2021); Version 6 (2025) - Expanded coverage (AGB for 2007, 2010, 2015-2022, plus change and uncertainty layers) (Santoro & Cartus, 2025; ESA CCI, (n.d.-a); ESA CCI, 2025a; Santoro, 2024).

ESA CCI Land Cover

The ESA Climate Change Initiative (CCI) Land Cover dataset provides consistent, global annual maps of land cover spanning 1992–2022 at 300 m spatial resolution, designed to support climate modeling and environmental monitoring (ESA CCI Land Cover, 2017; ESA CCI, (n.d.-b); Li et al., 2018). The product harmonizes multiple Earth observation missions, including AVHRR, MERIS, SPOT-VGT, PROBA-V, and Sentinel-3 OLCI/SLSTR, into a unified time series using the CCI Land Cover classification system aligned with the UN Land Cover Classification System (LCCS). The dataset is generated by fusing calibrated surface reflectance, top-of-canopy vegetation indices, and ancillary variables (e.g., DEM, climatology) into a supervised classification framework. Time-series compositing reduces cloud contamination, followed by machine-learning classifiers (e.g., random forests) trained on an extensive global reference database. Post-processing enforces spatial-temporal consistency, minimizing false land cover transitions across years (Li et al., 2018). Cross-calibration between different sensors ensures temporal stability despite evolving input missions.

Strengths: The ESA CCI Land Cover dataset offers a long-term, consistent global record with sufficient resolution (300 m) for regional assessments while remaining computationally feasible for global modeling. The dataset's annual temporal frequency supports trend analysis of land cover change over nearly three decades. Its compatibility with the LCCS and inclusion of per-pixel confidence layers facilitate integration with climate models, biodiversity assessments, and land-use change studies. Additionally, the multi-sensor integration improves classification robustness under varying atmospheric and seasonal conditions.

Weaknesses: Classification accuracy varies by biome, with lower performance in spectrally similar or heterogeneous landscapes such as savannas, wetlands, and mosaics of cropland and natural vegetation. The reliance on optical sensors means persistent cloud cover can reduce effective observations, despite compositing. Changes in sensor characteristics over the time series, although corrected, may still introduce residual inconsistencies.

Access: The ESA CCI Land Cover dataset is openly available via the ESA CCI Open Data Portal, delivering annual global land cover maps (300 m resolution, NetCDF & GeoTIFF) with full documentation (user guides, ATBDs, classification legends). Extended coverage (to 2020) is also hosted on the Copernicus Climate Data Store (CDS). Archived and citable versions for 1992–2015 (Version 2.0.7) are available via CEDA. All data are licensed under Creative Commons Attribution 4.0 (CC BY 4.0).

Radar backscatter dataset

Tao et al. (2023) present LHScat (Long-term, high-resolution scatterometer backscatter dataset), a global, long-term, monthly C-band radar backscatter dataset from 1992 to 2022-plus, at ~8.9 km spatial resolution, by harmonizing ERS-1/-2 (C-band), QSCAT (Ku-band), and ASCAT (C-band) signals via pixel-wise rescaling and decision-tree climate-based corrections (rainfall, skin temperature, snow depth). Validation against ESA ERS-2 (1995–2011) yielded high fidelity (regional Pearson r 0.79–0.98). A tropics focused version (1992-2018) has been used in applications such as analyzing drought impacts on rainforests (Tao et al., 2022).

Strengths: Long-span, high resolution, C-band robustness, global coverage, with regular updates as ASCAT continues. C-band is barely affected by clouds.

Weaknesses: Mainly reflects upper canopy water content. It has potential biases from the modeled QSCAT gap. The terrain effects are not directly corrected. Water bodies excluded via mask. The interpretation of backscatter in ecological terms remains model-assisted.

Access: Information is available through paper of Tao et al., 2023 as the available data. The tropics focused study (Tao et al., 2022) is available and the Github scripts and dataset.

1.2 GROUND-BASED DATA

Ground-based observations are determinant for quantifying and validating ecosystem resilience as they resolve processes and legacies that satellites infer only indirectly. Tree-ring chronologies archive multi-decadal growth responses to disturbances such as drought and heat, enabling explicit estimates of resistance, recovery rate, and memory effects. Eddy-covariance fluxes of GPP (gross primary productivity) and NEE (net ecosystem exchange) provide sub-daily to seasonal dynamics of carbon uptake and loss, allowing

detailed attribution to stress and meteorological drivers. Forest inventories datasets provide direct-field systematic records of tree and ecosystem attributes, but generally with very partial spatial coverage, and coarse temporal resolution (e.g. 5-10 years). A detailed description of dataset characteristics is provided in Table 5.

Table 5 Characteristics of Datasets products Ground-based data

Ecosystem variables	Dataset	Spatial resolution	Temporal resolution	Coverage	Time Span	Remarks
Tree ring data	ITRDB	-	Yearly	over 5000 sites		In situ
GPP, NEE	FLUXNET	-	Daily	212 sites		In situ
Forest Inventories		-	Variable			In situ

1.2.1. Tree-Ring Chronologies

ITRDB (Tree-Ring Data)

The International Tree-Ring Data Bank (ITRDB) is the world's largest public archive of tree-ring data, curated by the U.S. National Centers for Environmental Information (NCEI) and the World Data Service for Paleoclimatology. Established in 1974, it stores raw ring-width measurements, derived chronologies, and metadata contributed by dendrochronologists globally (Grissino-Mayer & Fritts, 1997; NOAA NCEI, 2023). As of 2023, the ITRDB contains over 5,000 sites across all inhabited continents, with particularly dense coverage in North America, Europe, and parts of Asia. Data originate from increment cores or cross-sections collected from living trees, remnant wood, or subfossil samples. Ring widths are measured to ±0.001 mm precision, then cross-dated to ensure accurate year assignments. Standardization removes age-related growth trends, producing ring-width indices that reflect interannual to centennial environmental variability (Cook & Kairiukstis, 1990). Chronologies may represent single species or multispecies composites for a site. Temporal resolution is annual, with many chronologies extending over several centuries. The longest exceed 8,000 years (e.g., bristlecone pine in the U.S. Southwest). Spatial resolution is determined by site distribution, point-based, typically at sub-kilometer precision, but geographically uneven.

Strengths: The ITRDB offers unparalleled temporal depth for terrestrial climate and ecological reconstructions, with annually resolved, exactly dated records. It supports diverse applications, including climate reconstruction, disturbance history, dendroecology, and model validation. The open-access policy and standard data formats (Tucson .rwl) facilitate reproducibility and integration with other paleoclimate archives.

Weaknesses: Spatial coverage is biased toward mid-latitude regions in the Northern Hemisphere, with sparse representation in the tropics, Southern Hemisphere, and remote boreal areas. Species selection often targets long-lived, climate-sensitive taxa, limiting representativeness for all forest types. Chronology standardization methods can remove low-frequency variability, complicating detection of long-term trends. Metadata completeness varies, and not all datasets include raw measurements.

Access: The ITRDB is hosted at NOAA's Paleoclimatology Data Center, where users can search by location, species, or investigator. Data are provided in .rwl, .crn, and associated metadata formats, under open-use terms with citation of original contributors.

1.2.2. Carbon Fluxes via **FLUXNET** (GPP/NEE)

The FLUXNET network is a globally coordinated collection of micrometeorological tower sites measuring exchanges of carbon dioxide (CO_2), water vapor (H_2O), and energy between terrestrial ecosystems and the atmosphere using the eddy covariance technique (Baldocchi et al., 2001; FLUXNET, 2020). Initiated in the late 1990s, it integrates regional networks such as AmeriFlux, EuroFlux, AsiaFlux, OzFlux, and others into a harmonized data infrastructure. As of 2023, FLUXNET comprises over 1,000 sites in more than 30 countries, spanning major climate zones and ecosystem types, from tropical rainforests to boreal tundra. At each site, high-frequency (typically 10–20 Hz) measurements of vertical wind velocity and scalar concentrations (CO_2, H_2O) are collected using infrared gas analyzers and sonic anemometers. The raw data are processed to compute turbulent fluxes via Reynolds decomposition, applying corrections for density effects (WPL correction), sensor separation, and coordinate rotation. Gap-filling of missing data and flux partitioning into gross primary production (GPP) and ecosystem respiration (Reco) follow standardized algorithms (e.g., the FLUXNET2015 and ONEFlux pipelines; Pastorello et al., 2020). Ancillary variables, such as meteorological drivers, radiation, and soil moisture, are also included. Temporal resolution is half-hourly or hourly, aggregated to daily, monthly, or annual time steps. Spatial resolution is footprint-scale, generally ~1 km^2, defined by tower height and atmospheric conditions.

Strengths: FLUXNET provides direct, continuous, in situ measurements of ecosystem-atmosphere exchanges, enabling detailed study of carbon, water, and energy budgets. Its standardized processing protocols ensure comparability across sites and time periods. The global network's diversity of ecosystems allows for robust empirical upscaling, satellite validation, and model benchmarking. High temporal resolution supports analysis of diurnal to interannual variability and extreme event responses.

Weaknesses: Spatial coverage is biased toward temperate and accessible regions, with underrepresentation of tropical, arid, and high-latitude biomes. The footprint-scale nature limits extrapolation without auxiliary modeling. Data gaps occur due to instrument failure or adverse conditions, and gap-filling introduces uncertainty. Long-term continuity is challenged by site funding cycles and changing instrumentation. Complex terrain and heterogeneous landscapes can violate assumptions of the eddy covariance method, affecting flux accuracy.

Access: Harmonized datasets, including FLUXNET2015 and subsequent releases, are available via the FLUXNET data portal in NetCDF format, with both open-access and restricted-use tiers. Metadata, quality-control flags, and uncertainty estimates accompany each record.

1.2.3. Forest Inventories

Forest inventory datasets provide systematic, ground-based records of tree attributes (e.g., diameter, height, species, mortality), serving as essential benchmarks for forest ecology, biomass estimation, and remote sensing validation. Their design, coverage, and accessibility vary considerably across regions. National Forest Inventories (NFIs) are the cornerstone of forest inventory data. They employ statistically representative, often permanent plots established on systematic grids (e.g., ~1 plot per 4–10 km²) to estimate stand structure and dynamics. In Europe, NFIs have been harmonized through EU-Forest initiatives under COST/EUFORGEN and Forest Europe (Tomppo et al., 2010). The US Forest Inventory and Analysis (FIA) program monitors ~355,000 plots on a ~2.5 km grid, measured every 5–10 years (O´Connell et al. 2024). Globally, FAO's Forest Resource Assessment (FRA) aggregates NFI data submitted by countries, providing coarse (~country-level) statistics every 5 years (MacDicken, 2015). At finer scales, plot networks such as ForestPlots.net or RAINFOR/AFRITRON maintain consistent protocols for tropical forests, supporting aboveground biomass and carbon dynamics assessments (Lopez-Gonzalez et al., 2011). Spatial resolution varies from plot-scale (~0.05–1 ha) to national grids (~10–100 km spacing), while temporal resolution is determined by remeasurement intervals (typically 5–10 years for NFIs). Continental compilations (e.g., EU-Forest) achieve pan-European coverage, while tropical plot networks provide patchy but intensively monitored sites. The FRA operates at the national scale with 5-year cycles.

Strengths: Direct, field-measured structural and taxonomic data provide unparalleled accuracy for biomass, carbon, and biodiversity assessment. Permanent plots enable detection of long-term demographic processes and disturbance effects. NFI harmonization initiatives (e.g., COST Action E43) have improved cross-country comparability, and plot networks support global remote sensing validation.

Weaknesses: Spatial representativeness is uneven, with dense coverage in temperate regions but sparse sampling in the tropics. Differences in measurement protocols, definitions (e.g., minimum DBH), and plot designs hamper cross-country consistency (Köhl et al., 2006). Limited public accessibility, as many NFIs are partially restricted due to national policy, which restricts open science. Coarse temporal resolution (multi-year cycles) limits near-real-time monitoring.

Access: Open NFI data are increasingly available (e.g., US FIA public database; selected European NFIs via EU-Forest data portal; ForestPlots.net for tropical networks). The FAO FRA datasets are freely accessible for all countries, though at aggregated levels.

2. DRIVERS OF VEGETATION DYNAMICS

Vegetation dynamics emerge from the interplay of multiple forcing variables, including climatic, biogeochemical, disturbance, and anthropogenic drivers. These factors regulate ecosystem functioning and condition the occurrence and impacts of extreme events such as droughts and heat waves. Table 6 inventories the main datasets representing these drivers (e.g., temperature, precipitation, vapor pressure deficit and fire occurrence), providing for each their spatial and temporal resolution, geographic coverage, temporal range, and associated strengths and weaknesses. These datasets can also be used to derive indices characterising droughts and heat waves, such as the Standardized Precipitation Evapotranspiration Index (SPEI) or Heat Wave Magnitude Index (HWMI), which are valuable when addressing the drivers of vegetation dynamics and compound events impacts on vegetation (Han et al, 2023; Barriopedro et al., 2023).

Table 6. Characteristics of datasets of drivers of vegetation dynamics

Drivers	Dataset	Spatial resolution	Temporal resolution	Coverage	Time Span	Remarks
Land surface temperature	CCI LST	1 km	Daily	Global	1996 - 2020	
Surface air temperature	ERA5-land	0.1°	Hourly	Global	1950 - present	
Surface air temperature	ERA5	0.25°	Hourly	Global	1940 - present	
Precipitation	ERA5	0.25°	Hourly	Global	1940 - present	
Precipitation	GPCC	0.25°	Monthly	Global	1891 - present	
Precipitation	GPCP Monthly 2.3	2.5°	Monthly	Global	1979- present	
Precipitation	GIRAFFE	1.0°	Daily	Global	2000-2022	
Vapour pressure deficit	ERA5	0.25°	Hourly	Global	1940 - present	
CO_2	CCI GHG	5°	Monthly	Global	2014 - 2023	OCO-2 FOCAL
Soil properties	ISRIC_SoilGrids	250 m	Static	Global	-	Soil organic carbon, soil type, volumetric water content at different pressure heads
Soil Moisture	CCI Soil moisture	0.25°	Daily	Global	1978 - 2023	

Groundwater	G3P (GRACE,GRACE-FO)	0.5°	Monthly	Global	2002-present
Terrestrial Water Storage	GRACE,GRACE-FO (ICGEM)	~2°	Daily-Monthly	Global	2002-present
Burned area	Fire CCI51	250 m	Monthly	Global	2001-2020
Burned area	MCD64A1	500 m	Monthly	Global	2001-2024
Burned area	VNP64A1	500 m	Monthly	Global	2012-2025
Burned area	Portugal Fire Atlas	30 m	Monthly	Portugal	1984-2024
Fire Radiative Power	MCD14ML	1 km	4 times daily	Global	2001-2024
Fire Radiative Power	VNP14IMGML	750 m	2 times daily	Global	2012-2025
Fire Radiative Power	LSA-502	>4 km	Every 15 min	Hemispherical	2004-2025
Tree-ring Fire scar network			Yearly	Western USA	
Disturbances		1 km	Yearly	Global	2001-2022

2.1 LAND SURFACE CLIMATE

ERA5 and ERA5-Land – air temperature, precipitation and vapour pressure deficit (VPD)

Among the most widely used sources, the ERA5 and ERA5-Land reanalysis datasets provide consistent, high-resolution climate variables (e.g., temperature, precipitation, and vapor pressure deficit) suitable for assessing vegetation–climate interactions, both produced by the European Centre for Medium-Range Weather Forecasts (ECMWF) as part of the Copernicus Climate Change Service (CCS).

ERA5 is the fifth generation ECMWF reanalysis for the global climate and weather for the past 8 decades. Data is available from 1940 onwards. ERA5 replaces the ERA-Interim reanalysis. ERA5 provides hourly estimates for a large number of atmospheric, ocean-wave and land-surface quantities. Key near-surface variables include 2 m air temperature (T2m), precipitation, and vapour pressure deficit (VPD), delivered at hourly temporal resolution and 0.25° spatial resolution. An uncertainty estimate is sampled by an underlying 10-member ensemble at three-hourly intervals. Ensemble mean and spread have been pre-computed for convenience. Such uncertainty estimates are closely related to the information content of the available observing system which has evolved considerably over time.

The **ERA5-Land** dataset provides global high-resolution reanalysis of land variables from January 1950 to present. Key near-surface variables include 2 m air temperature (T2m), precipitation, and vapour pressure deficit (VPD), delivered at hourly temporal resolution and 0.1° (~9 km) spatial resolution (Muñoz-Sabater et al., 2021). ERA5-Land is dynamically

downscaled from the ERA5 reanalysis using the ECMWF Integrated Forecasting System (IFS) with land-specific parameterizations and finer resolution. The system assimilates a wide range of meteorological observations (surface stations, radiosondes, satellites) through a 4D-Var scheme in ERA5, then applies land-surface modeling with the HTESSEL scheme to improve representation of soil moisture, snow, and surface energy fluxes. Precipitation is generated from model physics constrained by observations, while T2m is diagnosed at the model surface. VPD is not a native variable but computed from ERA5-Land air temperature and dewpoint temperature using the Clausius–Clapeyron relation.

Strengths: ERA5 and ERA5-Land offer a consistent, multi-decadal, hourly, high-resolution record suitable for hydrological, ecological, and agricultural applications. The ERA5-Land 9 km grid captures fine-scale variability better than coarser reanalyses (e.g., ERA5 ~31 km), and the land-specific tuning improves surface climate representation. The continuous temporal coverage facilitates climate trend analysis, extreme event characterization, and model forcing. Open, near-real-time access enables both retrospective and operational applications.

Weaknesses: As a reanalysis, ERA5-Land remains model-dependent, with biases in regions of sparse observational coverage (e.g., high mountains, parts of Africa). Precipitation accuracy is lower than in gauge-based datasets, particularly for convective events and snowfall. The downscaling does not assimilate additional land observations beyond those in ERA5, so improvements are largely from enhanced resolution and parameterization. VPD is derived from modeled humidity and temperature, thus inheriting uncertainties from both.

Access: ERA5 and ERA5-Land is openly available via the Copernicus Climate Data Store (CDS) (https://cds.climate.copernicus.eu) in NetCDF or GRIB format, with hourly or aggregated monthly data. Documentation includes product user guides, algorithm descriptions, and uncertainty assessments.

CCI Land Surface Temperature (LST)

The ESA CCI Land Surface Temperature (LST) dataset provides a consistent, long-term, global record of surface skin temperature derived from thermal infrared (TIR) satellite observations, supporting climate research and model evaluation (Ghent et al., 2024; ESA CCI LST, 2023; ESA CCI, 2023b). The most recent release covers 1995–2021 at daily temporal resolution and 0.05° (~5 km) spatial resolution, with separate day and night fields. The dataset is produced from multiple TIR sensors, including the Along-Track Scanning Radiometer series (ATSR-2 and AATSR on ERS-2 and Envisat) and the Moderate Resolution Imaging Spectroradiometer (MODIS on Terra/Aqua), merged into a harmonized climate data record. The retrieval algorithm applies split-window techniques to dual-view or multi-channel radiances to estimate LST, correcting for atmospheric water vapor, surface emissivity, and cloud contamination. Inter-sensor calibration and harmonization are implemented using overlapping observation periods, and a rigorous quality-control framework removes residual cloud and aerosol effects. The dataset provides per-pixel uncertainty estimates following GCOS climate monitoring principles (Ghent et al., 2024).

Strengths: The CCI LST dataset offers multi-sensor continuity over more than 25 years, enabling the detection of long-term surface temperature trends. The global coverage and separate day/night retrievals facilitate analyses of diurnal temperature variations and land–atmosphere interactions. Its adherence to GCOS Essential Climate Variable (ECV) standards ensures traceability, well-characterized uncertainties, and interoperability with other CCI datasets (e.g., soil moisture, vegetation indices). Validation against in situ radiometric measurements demonstrates high accuracy under clear-sky conditions.

Weaknesses: The reliance on TIR observations restricts retrievals to cloud-free conditions, potentially biasing climatologies in persistently cloudy regions (e.g., tropics). The 5 km spatial resolution limits application in heterogeneous urban and coastal environments. Sensor drift and varying overpass times between platforms require careful homogenization, and residual differences between sensors may remain despite inter-calibration. Moreover, LST measures skin temperature, which may differ significantly from near-surface air temperature, especially in sparse vegetation or arid regions.

Access: The ESA CCI LST dataset is freely available via the ESA CCI Open Data Portal and CEDA, with products in NetCDF format, user guides, algorithm theoretical basis documents, and uncertainty layers. Data is released under a Creative Commons BY 4.0 license.

GPCC Precipitation (Gauge-Based Gridded Analysis)

The Global Precipitation Climatology Centre (GPCC) provides high-quality gauge-based gridded precipitation analyses over global land areas (Rudolf et al., 2013; Schneider et al., 2022). The flagship Full Data Monthly Product (FD-MP, version 2022) offers monthly precipitation totals on multiple available spatial grids, 0.5°, 1°, 2.5°, and 0.25°, spanning 1891 to present, derived from approximately 86,000 rain gauge stations worldwide (Schneider et al., 2022; GPCC, 2025). GPCC aggregates station-based precipitation reports (e.g., CLIMAT, SYNOP) into a consistent dataset, which is quality controlled and interpolated via ordinary block kriging to create global grids. For daily resolution, the First Guess Daily Product (FG-DP, version 2022) provides estimates at 1° resolution with additional metadata such as standard deviation, interpolation error, and number of used stations (Schamm et al., 2014).

Strengths: As the longest and most comprehensive gauge-only product, GPCC Full Data Monthly offers unparalleled temporal depth (over 130 years), essential for climate change and water balance studies. Its foundation on real observations, without reliance on satellite retrievals, enhances data realism. Provision of uncertainty estimates (e.g., standard deviation, station density) supports robust scientific applications. Multiple spatial resolutions allow users to select an optimal scale for regional or global modeling efforts.

Weaknesses: The station network evolves over time, leading to inhomogeneous spatial coverage, dense in Europe/North America but sparse in parts of Africa and Asia, which can affect trend detection. Kriging-based interpolation may smooth extreme localized precipitation and fail under complex terrain. The First Guess Daily Product relies on preliminary data with lower quality control, so it is less accurate than the monthly reanalysis.

GPCC does not correct for systematic gauge measurement errors; users must apply provided climatological correction factors manually (GPCC, 2025).

Access: GPCC datasets are openly accessible via the Deutscher Wetterdienst (DWD) GPCC Download Gate - DWD, and via platforms like NOAA/PSL THREDDS, or Climate Data Guide (NCAR) (GPCC, 2025). Products are available in NetCDF and ASCII formats, with documentation, uncertainty layers, and guidelines for citation provided alongside.

GPCP Monthly 2.3 (Global Precipitation Climatology Project)

The Global Precipitation Climatology Project (GPCP) Monthly Version 2.3 data record provides a consistent global precipitation analysis from January 1979 to present, gridded at 2.5° × 2.5° spatial resolution with monthly temporal resolution. It is part of NOAA's Climate Data Record (CDR) program and integrates satellite and gauge observations to exploit the strengths of each (Adler et al., 2016; UCAR Climate Data Guide, 2025). GPCP v2.3 merges precipitation estimates from passive microwave sensors (SSMI/SSMIS), geostationary and polar-orbit infrared instruments (e.g., GOES, TOVS), and in situ gauge analyses (GPCC v7). Merging involves bias-adjustment and inverse-variance weighting to produce spatially homogeneous monthly precipitation fields (Adler et al., 2018). This version incorporates improved cross-calibration during satellite transitions (e.g., SSMI to SSMIS, TOVS to AIRS) and leverages updated gauge data to correct previously observed spurious trends in oceanic precipitation (Adler et al., 2018).

Strengths: Provides long-term, globally complete precipitation coverage, essential for climate-scale trend, variability, and climatology studies. Enhances homogeneity across sensor changes, reducing artificial trends post-2002 (Adler et al., 2018). Includes uncertainty/error fields and CDR-level documentation, enhancing transparency and scientific reproducibility (NCEI metadata).

Weaknesses: Coarse resolution (2.5°) limits applicability for regional or high-resolution hydrological studies. Satellite input data transitions can still introduce subtle biases in specific regions or time periods. Notably, v2.2 had a negative bias post-2003 especially over oceans, partially mitigated in v2.3 but not fully eliminated (Adler et al., 2018). High-latitude precipitation remains uncertain due to IR limitations and sparse gauge coverage.

Access: The dataset is openly accessible through NOAA's NCEI portal, via direct download, THREDDS catalog, AWS S3, and cloud services, with full NetCDF-4 (CF-compliant) format, source code, and ATBDs available, from UCAR´s Climate Data Guide, and IRI Data Library (Columbia University), with interactive view.

GIRAFE (Global Interpolated RAinFall Estimate) — EUMETSAT SAF on Climate

The GIRAFE datasets provide global, gridded precipitation estimates combining passive microwave and infrared observations, with daily accumulation and monthly mean precipitation output. Covering January 2002 to December 2022 (with monthly updates

planned from early 2025), data are provided at 1° × 1° spatial resolution, with rare temporal or spatial gaps flagged (EUMETSAT SAF n Climate, 2024). GIRAFE products merge Level-2 microwave observations from low-Earth orbit (LEO) instruments such as SSM/I, SSMIS, TMI, AMSR-E, AMSR2, GMI, AMSU-B, MHS, SAPHIR, and ATMS (processed via HOAPS, PNPR-CLIM, PRPS), with geostationary infrared (IR) brightness temperatures from sensors like VISSR, SEVIRI, GOES-I/N, and ABI. The merging uses microwave estimates to calibrate high-temporal-resolution IR data, optimizing sampling of intermittent precipitation. Daily accumulations are produced, then aggregated to monthly means. Each output includes sampling uncertainty, observation counts, and quality flags such as snow/sea-ice indicators or data completeness metrics (EUMETSAT SAF on Climate, 2024).

Strengths: Global coverage with consistent daily and monthly precipitation data across land and ocean at 1° resolution, which is useful for climate, hydrology, and model evaluation applications. Sampling uncertainty estimates and multiple quality control layers (e.g., observation counts, snow/ice flags) enhance transparency and facilitate informed filtering. Combines high-frequency IR with microwave "truth" to better capture intermittent precipitation events.

Weaknesses: Coarse spatial resolution (1°) limits utility in localized hydrological or flash-flood applications, and may smooth out orographic or convective precipitation extremes. IR calibration depends on microwave availability; microwave coverage gaps, especially at high latitudes or over ocean, may introduce sampling biases. Potential residual inaccuracies in snow/ice conditions and false precipitation in West Africa wet season, though flagged, may affect interpretation in polar or cold regions.

Access: GIRAFE v1.0 is openly accessible via the CM SAF Web User Interface, and secondarily on the Copernicus Climate Data Store (CDS), distributed as NetCDF-4, following CF v1.7 and ACDD v1.3 conventions, with both daily accumulations and monthly means, plus ancillary uncertainty and quality-control fields (EUMETSAT SAF on Climate, 2024).

2.2 ATMOSPHERIC CO_2

ESA CCI GHG XCO_2 Dataset

The ESA Climate Change Initiative Greenhouse Gases (GHG-CCI) project produces high-quality global estimates of column-averaged dry-air mole fractions of atmospheric carbon dioxide (XCO_2), derived from satellite instruments including SCIAMACHY (2002–2012), GOSAT (from 2009), and OCO-2 (2014–present). These datasets are produced as Climate Research Data Packages (CRDPs), with the latest being CRDP5/CRDP6, now available via the CCI Open Data Portal and CEDA archive (ESA CCI, 2022; Reuter et al., 2023). XCO_2 retrieval relies on hyper-spectral radiance measurements in near-IR/SWIR CO_2 and O_2 absorption bands. The FOCAL algorithm (Fast Atmospheric Trace gas Retrieval) used for OCO-2 applies a simplified radiative-transfer model approximating multiple scattering, enabling efficient and accurate inversion of XCO_2 with per-sounding uncertainty estimates (Reuter et al., 2017). Other sensors use independent retrieval schemes suited to their

characteristics, all harmonized under ESA GHG-CCI processing standards (ESA CCI, 2022). XCO_2 is available at the satellite footprint level, approximately 2.25 km (along-track) × 1.29 km (across-track) for OCO-2, with data aggregated into Level-3 gridded products at 1° × 1° or 0.1° × 0.1° resolution and daily to monthly temporal intervals, depending on data density and product tier.

Strengths: The XCO_2 CCI dataset provides a long-term, multi-sensor harmonized global record, crucial for monitoring atmospheric CO_2 trends and regional source-sink fluxes. It includes per-point uncertainty and quality metrics, enabling robust use in inversion models. The FOCAL algorithm's efficiency allows generation of large-scale products essential for climate applications (Reuter et al., 2017; ESA CCI, 2022).

Weaknesses: Retrievals are limited to cloud-free, daytime scenes, leading to spatial and temporal gaps, particularly in high-latitude and tropical regions. Inter-sensor calibration is challenging, and residual biases remain despite harmonization. The retrievals are also sensitive to aerosols and surface albedo uncertainties.

Access: XCO_2 products are available through the Copernicus Climate Data Store (CDS) and CEDA, in NetCDF format, accompanied by documentation, algorithm basis documents, and uncertainty estimates (ESA CCI, 2022).

2.3 SOIL PROPERTIES

ISRIC_SoilGrids

ISRIC SoilGrids is a global digital soil mapping initiative developed by ISRIC - World Soil Information. It generates high-resolution maps of soil properties across six standard depths (0–5, 5–15, 15–30, 30–60, 60–100, and 100–200 cm) at approximately 250 m spatial resolution using machine learning techniques and extensive soil profile data (Hengl et al., 2017; ISRIC, n.d.). SoilGrids utilizes over 150,000 georeferenced soil profile observations from the World Soil Information Service (WoSIS) alongside more than 400 environmental covariate layers (e.g., climate, land cover, DEM) to model soil properties globally (Hengl et al., 2017; de Sousa et al., 2021). The system employs an ensemble of machine learning methods, including Random Forest and Gradient Boosting, to predict variables such as organic carbon, pH, clay/sand/silt fractions, bulk density, cation exchange capacity, coarse fragments, and depth to bedrock. Each prediction includes quantified uncertainty via 90% prediction intervals, enabling explicit error propagation in downstream analyses (Hengl et al., 2017; ISRIC, n.d.).

Strengths: SoilGrids achieves globally consistent maps at fine (~250 m) spatial resolution, supporting ecosystem modeling, carbon stock estimation, and land surface parameterization. The provision of uncertainty layers enhances transparency and supports more rigorous modeling. The system is updatable, allowing integration of new soil profiles to refine maps over time (ISRIC, n.d.).

Weaknesses: SoilGrids lacks a temporal dimension, the outputs represent a static snapshot and are not temporally explicit, so temporal trend analysis is not possible (GIS StackExchange, 2022). Prediction accuracy varies by property, with explained variance ranging roughly from 56% (e.g., coarse fragments) to 83% (e.g., pH) (Hengl et al., 2017). Sparse observational coverage in some regions (e.g., tundra, deserts) may reduce reliability in those areas. Additionally, compositional constraints (e.g., clay, silt, sand summing to 100%) require careful data handling when aggregating metrics.

Access: SoilGrids products are freely accessible under CC-BY 4.0 via the SoilGrids portal, Soil data hub and platforms like GEE Community Catalog, in GeoTIFF or NetCDF formats, with associated model metadata and uncertainty layers included (ISRIC, n.d.; de Sousa et al., 2021).

2.4 SOIL MOISTURE

ESA CCI Soil Moisture

The ESA Climate Change Initiative (CCI) Soil Moisture dataset provides a robust, harmonized Climate Data Record (CDR) of surface soil moisture (SSM) globally, integrating both active (radar) and passive (radiometer) satellite observations (Dorigo et al., 2017; ESA CCI Soil Moisture, n.d.). It produces three core products: ACTIVE, PASSIVE, and COMBINED, available as daily global grids at a 0.25° (~27 km) spatial resolution. The PASSIVE and COMBINED records span from 1 November 1978 to 31 December 2022, while the ACTIVE product covers from 5 August 1991 to 31 December 2022 (ESA CCI Soil Moisture, n.d.). The ACTIVE product merges scatterometer-based estimates (e.g., from AMI-WS, ASCAT) expressed in percent saturation, while the PASSIVE product combines radiometric datasets (e.g., SMMR, SSM/I, AMSR series, SMOS, SMAP, GPM) into volumetric moisture units (m^3/m^3). The COMBINED product fuses both using an optimal merging scheme with inter-sensor bias correction and consistency filtering. The merging process is underpinned by robust inter-calibration, quality control, and blending methodologies (Dorigo et al., 2017; Gruber et al., 2019; Preimesberger et al., 2021).

Strengths: This dataset offers a long-term, multi-decadal record of surface soil moisture with consistent spatiotemporal coverage, making it invaluable for climate trend analyses and hydrological modeling. The triad of products allows users to select either instrument-specific data (active or passive) or a merged dataset that balances spatial fidelity and temporal continuity. It is officially recognized and used in climate assessments (e.g., State of the Climate reports) and is available in near real-time operational mode via C3S (ESA CCI Soil Moisture, n.d.).

Weaknesses: Despite improved data continuity, spatial gaps remain due to revisit limitations or radio-frequency interference—particularly in dense vegetation or high-latitude areas. The coarse spatial resolution restricts fine-scale hydrological or ecological applications. Although the COMBINED record is bias-corrected, residual structural breaks arising from sensor transitions necessitate careful homogenization (Preimesberger et al., 2021).

Access: All products (ACTIVE, PASSIVE, COMBINED) are publicly accessible via the ESA CCI Soil Moisture project portal and the CEDA Archive in NetCDF-4 format, complete with metadata, quality flags, and algorithm documentation (ESA CCI Soil Moisture, n.d.).

2.5 GROUNDWATER & TERRESTRIAL WATER STORAGE

GRACE/GRACE-FO (Terrestrial Water Storage)

The GRACE (Gravity Recovery and Climate Experiment) mission (2002–2017) and its successor GRACE-FO (Follow-On; from 2018) provide monthly global maps of terrestrial water storage anomalies (TWSA) by measuring Earth's time-variable gravity field (Landerer et al., 2024). These measurements capture total changes in water stored in soils, aquifers, snow, and surface water bodies. Spatial and temporal resolution is approximately 300 km (effective after filtering) with monthly temporal coverage, dictated by the need to remove correlated errors and noise through spatial smoothing (Ghobadi-Far et al., 2024). Derivation involves measuring minute variations in the distance between twin satellites as they respond to changes in Earth's gravitational field caused by mass redistribution. These data are converted into surface mass change using spherical harmonic or mascon (mass concentration) solutions. The JPL RL06.3 mascon product applies regularization and bias correction, improving signal localization and reducing leakage errors (NASA JPL, n.d.).

Strengths: Include the dataset's unique ability to provide direct, global-scale observations of integrated water storage changes, enabling detection of regional to continental hydrological trends, drought events, and groundwater depletion (O'Neill & Chandler-Ho, 2021). The mascon approach offers reduced striping and improved interpretability compared with traditional spherical harmonics (NASA JPL, n.d.). The long-term continuity from GRACE to GRACE-FO facilitates multi-decadal climate analyses (Landerer et al., 2024).

Weaknesses: Its coarse spatial resolution, limiting utility for basin-scale water management or small aquifer monitoring (Ghobadi-Far et al., 2024). The dataset also suffers from signal leakage across hydrological boundaries and a data gap between missions (mid-2017 to mid-2018), though interpolation methods partly address this issue (Gerdener et al., 2023). Temporal resolution is restricted to monthly scales, making it unsuitable for short-term hydrological events.

Access: Open access via the NASA PO.DAAC (mascon products) and includes NetCDF formats, quality flags, and uncertainty estimates (NASA JPL, n.d.). Enhanced gap-filled datasets, such as GLWS2.0, merge GRACE/GRACE-FO with the WaterGAP model to produce continuous 0.5° monthly TWSA fields from 2003–2019 with quantified uncertainties (Gerdener et al., 2023).

GRACE-based G3P

The Global Gravity-based Groundwater Product (G3P) delivers monthly global estimates of groundwater storage anomalies (GWSA), derived through a mass-balance framework combining GRACE/GRACE-FO Terrestrial Water Storage (TWS) with other terrestrial water storage compartments (WSCs): soil moisture, snow water equivalent, glacier mass, and

surface water (Güntner et al., 2024). It offers a unique, satellite-based global perspective on groundwater variability from April 2002 to September 2023, at a 0.5° (~50 km) grid resolution (Güntner et al., 2024; IGRAC, 2025). G3P computes GWSA by subtracting WSC anomalies from GRACE-derived TWSA. Each WSC is obtained from existing Copernicus services or models and filtered with a 250 km Gaussian kernel to match GRACE's resolution. The product includes both the groundwater anomalies and uncertainty layers, which are derived through formal error propagation from TWS and each WSC uncertainty (Güntner et al., 2024; GravIS documentation, 2025).

Strengths: G3P fills a critical observational gap in global groundwater monitoring by providing consistent, observation-based monthly estimates over two decades. It is grounded in satellite data, avoiding over-dependence on models, and is globally complete (excluding Greenland and Antarctica). The inclusion of uncertainty estimates per grid cell enhances scientific rigor and applicability. G3P is co-designed to support groundwater drought indicators and to integrate within the Copernicus ECV framework for hydrology (Güntner et al., 2024; G3P project overview, 2025).

Weaknesses: The coarse spatial resolution (0.5°) limits its use for small-scale aquifers or local water management. The method relies on accurate WSC datasets—and residual errors or mismatches may propagate into GWSA. Filtering to match GRACE smooths sharp gradients, potentially damping strong regional changes. Coverage still excludes cryosphere-dominated regions like Antarctica, and data gaps or misestimations in individual WSC layers (e.g., snow water equivalent errors in June 2005) may affect specific months (GravIS, 2025).

Access: G3P v1.12 (the latest version) is publicly available from IHP-UNESCO dataset page, via GFZ Data Services, supplied as NetCDF files containing anomaly and uncertainty layers for each component, with global coverage and monthly time steps. Visual access and region-specific time series (e.g., river basins, aquifers) are available via the GravIS portal (Güntner et al., 2024; GravIS, 2025).

2.6 BURNED AREA

ESA FireCCI (Burned Area)

The ESA Climate Change Initiative (FireCCI) project delivers a global long-term burned-area (BA) dataset, capturing fire disturbance as an Essential Climate Variable (ECV). The FireCCI51 product, its most recent and widely recommended version, provides monthly pixel-level burned-area maps at ~250 m spatial resolution and aggregated gridded data at 0.25° resolution, covering the years 2001–2020 (ESA CCI, 2025b; Copernicus Climate Change Service, Climate Data Store, 2019). FireCCI51 combines MODIS surface reflectance (250 m) from Terra with active fire detections to delineate burned scars via a two-phase hybrid algorithm. First, high-confidence "seed" pixels are identified based on active fire hotspots; next, contextual expansion with adaptive thresholding identifies contiguous burned areas based on near-infrared (NIR) reflectance changes (Lizundia-Loiola et al., 2020). Each pixel includes metadata such as day-of-burn detection, confidence level, and burned land-cover

class derived from ESA's CCI Land Cover dataset (Copernicus Climate Change Service, Climate Data Store, 2019).

Strengths: FireCCI51's high spatial resolution (~250 m) enables fine-scale detection of fire scars beyond coarse climate models. Its long-term, consistent record (2001–2020) supports trend analyses, ecosystem modeling, and fire regime research (Otón et al., 2021). Pixel-level confidence metrics and land-cover context provide critical quality control. The two-phase algorithm improves accuracy by leveraging both spectral and active fire information, enhancing detection in heterogeneous landscapes (Lizundia-Loiola et al., 2020).

Weaknesses: As a passive optical product, FireCCI is limited to cloud-free conditions, leading to omissions where cloud cover is persistent. Differentiating burned areas in croplands and agricultural mosaics is challenging, potentially inflating omission errors (Otón et al., 2021). Comparisons across different product versions (e.g., AVHRR-based FireCCILT11 vs. MODIS-based FireCCI51) reveal discrepancies due to sensor differences, requiring careful harmonization for long-term trend analysis (Otón et al., 2021). For more details see Franquesa et al. (2022).

Access: FireCCI51 products (Pixel and Grid) are openly accessible via the Copernicus Climate Data Store, the ESA CCI Open Data Portal, and Google Earth Engine. Data is offered in NetCDF or GeoTIFF format, with documentation, algorithm theory, and usage guidance included (ESA CCI, 2025b; Copernicus Climate Change Service, Climate Data Store, 2019).

MCD64A1 (MODIS Burned Area, Collection 6.1)

MCD64A1 delivers global burned-area maps at 500 m spatial resolution on the MODIS sinusoidal grid, produced monthly from November 2000–present. Each monthly tile includes the per-pixel burn date (Julian day-of-year), a burn date uncertainty layer (in days), and QA flags. Inputs are daily MODIS 500 m surface reflectance (Terra+Aqua) and 1 km MODIS active-fire detections; outputs are distributed as HDF-EOS with tile-level metadata (Giglio et al. 2018; LP DAAC User Guide v6/6.1). The Collection 6/6.1 hybrid algorithm computes a burn-sensitive SWIR vegetation index from MODIS bands 5 and 7, and temporal texture. It applies dynamic thresholds and uses cumulative active-fire maps to guide training/prior probabilities and contextual relabeling. Burn date is assigned to the nearest day; QA bits document mapping conditions (e.g., shortened mapping window) (Giglio et al., 2018; MODIS BA User Guide).

Strengths: Relative to earlier MODIS products, C6 detects substantially more burned area and smaller burns, with reduced omission error and improved temporal reporting (e.g., 44% same-day, 68% within two days of active-fire detections). Extensive Stage-3 validation against Landsat reference data quantifies aerial accuracy and uncertainties. These attributes have made MCD64A1 the backbone for derived fire datasets (e.g., GFED, Global Fire Atlas) (Giglio et al., 2018; Boschetti et al., 2019; Andela et al., 2019/2024 notes).

Weaknesses: At 500 m and monthly compositing, MCD64A1 can miss fine-scale or low-severity/understory fires and exhibits regional biases under persistent cloud, snow/ice,

or agricultural burning. Cross-product intercomparisons show non-negligible disagreements with alternative burned-area series, especially at local scales; careful use of QA/uncertainty layers and aggregation is recommended (Humber et al., 2019; Boschetti et al., 2019).

Access: Open access via NASA LP DAAC, also available in Google Earth Engine with full metadata and processing script support. The LP DAAC provides cloud (LPCLOUD) endpoints; UMD distributes reprojected GeoTIFF/Shapefile variants noted in the user guide (LP DAAC product page & news; LAADS; User Guide).

VNP64A1 (VIIRS Burned Area, Collection 2)

VNP64A1 delivers global burned-area data at 500 m spatial resolution (after resampling from native VIIRS 750 m) on the MODIS sinusoidal grid, with monthly temporal resolution, spanning March 2012 to present (Giglio et al., 2024). Each pixel includes a burn date (day-of-year), uncertainty estimate, first/last reliable observation days, and QA flags indicating data confidence and mapping conditions (Giglio et al., 2024; LP DAAC, 2019). The algorithm employs a hybrid approach, leveraging VIIRS daily surface reflectance time series (bands M8 and M11) to detect abrupt spectral changes indicative of burn scars, complemented by active-fire detections to guide classification. Dynamic thresholds and temporal textural metrics are applied to identify post-fire recovery signals, with active-fire data serving as prior probabilities and contextual validation. Burn dates are assigned using the nearest possible observation, and flag layers document cloud cover, snow, or algorithm conditions (Giglio et al., 2024).

Strengths: Offers higher spatial detail than MODIS burned-area products (e.g., MCD64A1), enhancing detection of smaller and fragmented burn events. Monthly global coverage provides consistent long-term monitoring of fire regimes across diverse ecosystems. Comprehensive QA and uncertainty layers facilitate critical filtering and uncertainty-aware analyses. Built on robust VIIRS sensor capabilities, with superior signal-to-noise performance and enhanced spectral bands for fire detection.

Weaknesses: Temporal resolution is monthly, limiting capacity to resolve intra-month fire progression or short-duration events. Native 750 m resolution resampled to 500 m may not fully capture sub-pixel heterogeneity in fire severity or extent. Persistent cloud cover, snow, or rapid vegetation regrowth may obscure burns, despite QA flags and masking. As a nascent product, comprehensive validation studies comparable to MODIS BA products may still be emerging.

Access: VNP64A1 Collection 2 is openly available through NASA LP DAAC, distributed as HDF-EOS5 formats. The dataset is also hosted in Google Earth Engine, with detailed methodology and usage notes provided in the User's Guide and Algorithm Theoretical Basis Document (ATBD) (LP DAAC, 2019; Giglio et al., 2024).

Portuguese Fire Atlas

The Portuguese Fire Atlas is a set of burnt area maps for mainland Portugal over 40 years (1984-2023) with monthly temporal resolution, derived from Landsat imagery (Neves et al., 2023). It has a spatial resolution of 30 m. Neves et al. (2023) improved the temporal resolution of the burnt area maps by disaggregating the burnt area patches of the previous version of the Fire Atlas (Oliveira et al., 2011) into individual events, dated with a monthly step. This improves the assessment of intra-annual fire variability in Portugal. Covering a period of 40 years, it allows the long-term analysis of changes in fire regimes in Portugal, which might have been substantial, driven by changes in rural area demographics and land use. The fire atlas is also essential for the development of fire susceptibility maps for Portugal (e.g. Oliveira et al., 2021).

Strengths: The long-term coverage (40 years) and the spatial resolution of 30 m, much higher than those of the global burnt area products. Compared to the previous version of the atlas (Oliveira et al., 2011), which had an annual temporal resolution, the monthly temporal resolution of this atlas allows the analysis of fire seasonality.

Weaknesses: Burnt area dating accuracy depends on the number of available images, which fluctuates according to the Landsat satellite and cloudiness of each year (Neves et al., 2023). The Atlas typically underestimates the area that burnt outside the summer season. A new version of the Atlas is under development, which will be produced using all the Landsat images available, and will improve the burnt area mapping during the winter months. This will allow the obtention of separate trends for winter/spring fires (pastoral burning) and summer wildfires, which is important for fire management.

Access: The Portuguese Fire Atlas is available in PANGAEA.

2.7 FIRE RADIATIVE POWER

MCD14ML

MCD14ML is the global monthly list of MODIS active-fire detections that merges Terra and Aqua overpasses and reports, for each 1 km pixel, geolocation, detection time, confidence, brightness temperatures (T4/T11), and fire radiative power (FRP; MW) (contextual algorithm from 4 µm and 11 µm radiances). Spatial resolution is the nominal 1 km MODIS pixel at nadir and temporal resolution is per overpass detection (up to ~4/day locally; Terra ~10:30/22:30, Aqua ~13:30/01:30 LT), distributed as monthly files (MCD14ML) (Giglio, 2021; Giglio et al., 2016; FIRMS, 2024). Candidate “hot” pixels are identified by a contextual test against a dynamically modeled background using MODIS 4 and 11 µm radiances. After quality screens, FRP is estimated from the excess MIR radiance above background following Wooster et al (2003) MIR-radiance approach, providing a physically based proxy for instantaneous combustion rate and fire intensity (MW) (Giglio et al., 2016; Wooster et al., 2005).

Strengths: Global, consistent, long record (2000–present) enabling climatologies, diurnal/day–night contrasts, and emission modeling; Pixel-level FRP offers a quantitative intensity proxy tightly linked to fuel consumption and smoke emissions. Rapid access via NRT

MCD14DL with later replacement by standard MCD14ML improves both timeliness and quality (Giglio, 2021; Giglio et al., 2016; Vadrevu et al., 2018).

Weaknesses: Mixed-pixel effects at 1 km: small or low-intensity fires may be missed and FRP can be biased by sub-pixel flame area. Screening gaps (cloud, smoke, glint, high surface temperature, extreme view angles) lead to omission/commission errors and diurnal biases. MCD14ML monthly lists lack explicit cloud/no-observation masks, so naïve fire-counting can be misleading unless observation gaps are handled. Sensor saturation and daytime background heating can bias FRP for extreme events (Giglio, 2021; Giglio et al., 2016).

Access: Standard MCD14ML (CSV/SHP) can be downloaded from FIRMS (archive) with ~2–3-month latency. NRT MCD14DL is available within hours on earthdata and later replaced by the standard archive. Original products and documentation are at the MODIS Active Fire & Burned Area (UMD) site. Swath/Level-2 HDF and related products are also at LAADS/LP-DAAC (FIRMS, 2024; MODIS GSFC page).

VNP14IMGML

VNP14IMGML is the monthly global list of VIIRS 375 m (I-band) active-fire detections from Suomi-NPP, reporting per-pixel geolocation, detection time, quality/confidence, and FRP (MW) derived for each detection (Schroeder et al., 2014; Schroeder et al., 2024). Spatial resolution is the nominal 375 m VIIRS pixel at nadir. Detections occur per satellite overpass (~01:30 and ~13:30 local time for S-NPP; ~2/day), with records aggregated into monthly text files (NASA VIIRS Land Team, n.d.; LAADS DAAC, n.d.). VIIRS active-fire detection uses a contextual algorithm on mid-IR/thermal signals that models a local background and flags anomalously hot pixels (Schroeder et al., 2014). For FRP, the operational VIIRS 375 m product uses the co-located 750 m dual-gain M13 (~4 µm) radiance to avoid I4 saturation. The excess MIR radiance above background is converted to FRP following Wooster et al. (2003) radiance–FRP relationship (NOAA JPSS, 2019; Schroeder, 2024). The result is an instantaneous, physically-based proxy for combustion rate attached to each active-fire pixel.

Strengths: Higher spatial detail (375 m) than MODIS (1 km) yields better small-fire sensitivity and more accurate localization (Schroeder et al., 2014). Per-detection FRP enables intensity/combustion assessments and improves emission modeling when integrated over time (Schroeder et al., 2024). Global, consistent, multi-year record (2012–present) with straightforward monthly access via text/CSV supports climatological and management applications (NASA FIRMS, 2024).

Weaknesses: Sub-pixel FRP: even at 375 m, FRP depends on fractional flame area and view geometry. Using 750 m M13 for FRP introduces scale-mismatch with 375 m detections (NOAA JPSS, 2019). Screening gaps (cloud, smoke, sunglint, extreme scan angles) and diurnal sampling (twice-daily) cause omission/commission biases and temporal aliasing. Monthly lists do not include explicit no-observation masks, so effort-normalization is essential (Schroeder et al., 2024). Saturation/background heating can bias daytime FRP for extreme events (Schroeder et al., 2014).

Access: The monthly VNP14IMGML files are downloadable from NASA FIRMS (CSV/SHP/JSON) and via LAADS/LP-DAAC. Historical distribution is also mirrored by the University of Maryland server documented in the user guides (NASA FIRMS, 2024; Schroeder et al., 2024; LAADS DAAC, n.d.).

LSA-502 Fire radiative power

LSA-502 is the per-pixel active-fire FRP product from EUMETSAT's LSA-SAF, generated from SEVIRI radiances on Meteosat-8/9/10/11. It lists each detected fire's location, detection time, confidence, FRP (MW) and uncertainty. Spatial resolution is ~3 km at the sub-satellite point (coarser off-nadir). Temporal resolution is every 15 min at full disk. Coverage spans the Meteosat field-of-view (operational since 2008), with regional subsets over Europe, Africa and S. America sectors (Wooster et al., 2015; LSA-SAF, n.d.; EUMETSAT Navigator, n.d.). LSA-502 ingests Level-1.5 SEVIRI brightness temperatures and applies a geostationary Fire Thermal Anomaly (FTA) contextual test (3.9 µm vs. locally modelled background) to flag hot pixels. FRP is retrieved from the excess MWIR radiance above background using the Wooster MIR radiance–FRP relationship, yielding a physically based, instantaneous proxy for combustion rate (Wooster et al., 2015). The product also provides per-pixel FRP uncertainty and a confidence measure (Wooster et al., 2015; Roberts et al., 2015).

Strengths: High revisit (15 min) resolves diurnal fire behavior and intensity dynamics that polar imagers miss. Consistent, near-real-time geostationary stream supporting emissions modelling and assimilation. Physically grounded FRP comparable across space/time and linked to fuel consumption (Wooster et al., 2015; Roberts et al., 2015).

Weaknesses: Coarse pixels and limb effects reduce sensitivity to small/low-FRP fires and can bias FRP at large view angles. Cloud/smoke screening and sun-glint cause omission/commission errors. FRP is sub-pixel and depends on fractional flame area and background temperature. Geographic coverage is limited to the Meteosat disk (Wooster et al., 2015; Roberts et al., 2015).

Access: LSA-502 is distributed operationally and in archive via the LSA-SAF portal and EUMETCast in HDF5/NetCDF, with directories exposing 15-min granules. Product pages and documentation (ATBD, PUM, validation) are hosted by LSA-SAF, and some filtered feeds are also exposed via NASA FIRMS for Meteosat (LSA-SAF, n.d.; EUMETSAT Navigator, n.d.; NASA FIRMS, n.d.).

2.8 TREE-RING FIRE SCAR NETWORK

North American Tree-Ring Fire Scar Network (NAFSN)

NAFSN is a continent-scale compilation of site-level fire-scar chronologies from crossdated tree rings, assembled from >2,500 sites and >37,000 fire-scarred trees across North America

(Margolis et al., 2022). Each record identifies calendar year of burning and, from within-ring position, intra-annual season (dormant, early/late earlywood, latewood), yielding annual to sub-annual temporal resolution (Grissino-Mayer, 2001). The dataset's spatial resolution is site/plot-scale points (irregular locations with coordinates and site metadata). Within sites, scars are recorded at individual-tree (meters) scale rather than on a grid (NOAA NCEI, 2024). Network coverage spans 0–2019 CE with long chronologies concentrated between the 1500s and late 1800s (NOAA NCEI, 2024; Margolis et al., 2022). Investigators collect cross-sections/cores from fire-scarred trees, crossdate rings to exact years, assign seasonal position to scars, and compile site chronologies in standard FHX2/FHAES formats (Grissino-Mayer, 2001; NOAA NCEI, 2024). The NAFSN synthesis harmonizes contributed site files and metadata (species, years, number of trees, area sampled) into a unified archive (Margolis et al., 2022; NOAA NCEI, 2024).

Strengths: Multi-century, annually resolved records enable pre-suppression baselines, frequency/rotation analyses, and fire–climate synchrony studies. Seasonality coding constrains fire weather/phenology. Unparalleled sample size and continental coverage support robust spatial analyses and comparisons with modern satellites and management records (Margolis et al., 2022).

Weaknesses: Sampling heterogeneity (biome, ownership, accessibility) produces geographic gaps and regional biases. Fire-scar archives preferentially record non-lethal surface fires, and stand-replacing events may be underrepresented. Recording and survivorship biases (tree availability, scar visibility, variable sample depth through time) influence inferred frequencies. Seasonal assignment of dormant scars can be ambiguous without local cambial phenology (Grissino-Mayer, 2001; Margolis et al., 2022).

Access: The synthesis is distributed by NOAA NCEI (WDS Paleoclimatology) with a DOI and open CSV (site table), FHX2 site files, readme, and fire-history graphs (directory access). Site descriptions (location, species, years, area) are additionally cataloged via U.S. open-data portals (NOAA NCEI, 2024; U.S. Data.gov, 2024).

2.9 DISTURBANCES

Global Drivers of Forest Loss

This dataset provides a global, spatially explicit attribution of dominant drivers behind tree-cover loss from 2001 to 2022, delivered at ~1 km spatial resolution (0.01°) (Sims et al., 2025). Built upon the Global Forest Change (GFC) loss maps (Hansen et al., 2013), the dataset applies a deep-learning framework (ResNet CNN) trained on ~7,000 high-resolution human-interpreted samples to classify seven driver categories: permanent agriculture, hard commodities, shifting cultivation, logging, wildfire, settlements/infrastructure, and other natural disturbances. Validation against independent samples yields ~90.5% overall accuracy (Sims et al., 2025).

Strengths: Global coverage, annual updates, and driver attribution at thematic detail sufficient for land-use monitoring, supply-chain accountability, and resilience modeling.

Weaknesses: One-driver-per-pixel assumption, dependence on the accuracy of GFC loss detection, and potential underrepresentation of fine-scale or overlapping disturbances (Sims et al., 2025).

Access: The dataset is openly available on Zenodo in GeoTIFF format (including probability layers and reference points) and via Google Earth Engine, distributed under a CC-BY-4.0 license (Sims et al., 2025).

3. TOOLS

3.1 RESILIENCE METRICS

We plan to benchmark resilience metrics with respect to their ability to reflect the restoring rate. The resilience metrics performance in this task is highly interlinked with the data set used for this task, and must thus be investigated also separately for each data set, i.e. we will identify ideal combinations of metrics and data.

The framework will extend the work by Smith et al. (2022). For a single data set, we will detect significantly large perturbations and calculate the recovery thereof as the best-fit exponent of an exponential function. This will be termed *empirical recovery rate*. In addition, we will for all these locations calculate the resilience metrics (see below) and compare them against the empirical recovery rates. If the metrics and the empirical recovery rate are close within each single grid cell, or location, one can conclude that the metric is capable of capturing recovery rate within the given data set. However, this implies that the metric is *only* influenced by the recovery rate and no other - potentially spatially varying - variables. From the resilience metrics listed in the Science Requirements Document, we will be able to benchmark

- auto-correlation and the λ derived from it
- the λ derived from variance when corrected for the influence of the noise amplitude
- λ derived via linear regression
- λ derived via linear regression under the assumption of auto-regressive noise , i.e. by Generalized Least Squared with AR covariance structure (GLSAR) suggested as a metric for resilience monitoring in the presence of autocorrelated noise by Boers (2021)
- λ derived via Kramers-Moyal

Moreover, the differences in the recovery rate across locations must be related to differences in resilience, compared to differences in the intrinsic time scales of the system. Thus, the comparison and benchmarking of resilience metrics and data sets must be evaluated separately for systems with different time scales, i.e. ecosystems.se

3.2 MODELS

Land surface and vegetation model LPJmL

We have access to the process-based land-surface and dynamical global vegetation model (DGVM) LPJmL (Schaphoff et al., 2018). The model is a state-of-the-art tool for assessing climate impacts on ecosystems and managed vegetation alike, and has also been used in a coupled Earth system model context (Drueke et al., 2021).

It can be forced by daily CO_2 concentration, temperature, precipitation, downwelling long-wave and short-wave radiation, and soil properties. Input data from (bias-corrected) ERA5 is available. Where possible, we will make use of already established setups and simulated data, e.g. from Bathiany et al. (2024) and Bathiany, Kim and Boers (2025). Bathiany et al. (2024) also established a model hierarchy derived from LPJmL, reaching from the original model to a highly simplified core of carbon dynamics and tree cover dynamics, respectively.

LPJmL and its derivatives are available to support the following activities where required:

1. Assessment of ecological resilience and space-for-time replacement (Task 2.4). Here, the model can be used in order to investigate whether multiple modes of environmental conditions (atmospheric variables like temperature or radiation, as well as soil-related parameters) can lead to multiple modes of tree productivity, and consequently, in tree cover. In contrast to the real world, the model allows disabling vegetation fires and related feedback, and hence assess mechanistic explanations unrelated to fire. A long stationary simulation for the Meso and South America domain (EXP1 in Bathiany et al., 2024) is already available and can be used in this context.
2. Assessment of the behaviour of different resilience metrics in the absence of observational uncertainties (Task T2). In a variety of simple vegetation models and versions of LPJmL, it can be assessed how well resilience metrics compare to actual resilience measured by the recovery rate. This allows a conceptual assessment of the applicability of certain metrics on certain (simulated) variables. Although the model does not capture all processes and all heterogeneity from the real world, it allows studying the reliability of resilience metrics in an idealised system without any observational uncertainties.
3. Attribution of observed trends to major drivers like climate change, CO_2 fertilisation, or internal variability (Task T3). The observed spatial differences of resilience and its trends over time at each location can be compared to model simulations of the historical period. Differences will likely occur due to limitations in process-representation and forcing. However, more general features like mean biomass, coverage or LAI can be attributed in the model by enabling and disabling climate trends in different variables, hence allowing a factor separation.
4. Assessment of uncertainties stemming from observing different parts of the soil-vegetation-atmosphere system with different weights in a signal like Vegetation Optical Depth (VOD) (Task T4). Unfortunately, observable vegetation indicators like NDVI or VOD are not represented in DGVMs. In turn, key variables in DGVMs like

vegetation carbon and soil carbon are very hard to observe. However, what can be done conceptually is to explore the potential role of different carbon pools and/or moisture (which have different intrinsic time scales) to contribute to multivariate indices, depending on their weight in a signal. This may support the understanding of epistemic uncertainties when interpreting an observed indicator (like VOD) in terms of a vegetation variable (like above-ground biomass).

3.3. Computing resources

The study of resilience in complex environmental systems requires high-performance computing (HPC) resources, as analyses often rely on large Earth observation datasets, machine learning models, and simulation-based frameworks. The computing resources available at each partner institution are summarized in Table 7. All partners have access to sufficiently powerful infrastructures to carry out the proposed objectives, ensuring both the computational intensity of deep learning approaches and the memory requirements of large-scale data integration are met. TU Munich (TUM) provides access to both exclusive and shared HPC facilities, including cutting-edge GPU nodes optimized for machine learning. TU Wien (TUW) contributes with a reliable CPU-based architecture suitable for large-scale simulations and preprocessing tasks. NPL hosts a heterogeneous configuration with state-of-the-art GPUs and very large memory, enabling advanced AI workflows and high-volume data handling. ULEIP offers both GPU-rich and CPU-rich systems, allowing flexibility across diverse computational demands. Finally, ULISB complements the infrastructure with a powerful workstation optimized for intensive experimentation and prototyping. Together, these resources provide a robust and complementary computing environment tailored to the project's resilience research goals.

Table 7. Distribution of the type of exclusive and shared hardware of each partner institution

Partner Institution	Exclusive hardware	Shared hardware
TUM	GPUs: 8 NVIDIA H200's, 8 NVIDA B200's	PIK HPC cluster, incl. >40 H100's LRZ, including >500 H100's and DKRZ Levante (extra application required)
TUW	CPUs: 2 x Xeon E5-2670 v3 @ 2.3 GHz, 12 Core	N/A
NPL	2 CPUs: 4 × NVIDIA A100 GPU-80 Gb, 2x AMD EPYC 7643 2.3GHz,1024 GB RAM 1 GPU: 2 × NVIDIA P100 GPU, 6 GB	N/A

	RAM per CPU (32 CPUs)	
ULEIP	GPU machine: - AMD EPYC 9554 64-Core Processor - 768GB RAM - 4x A6000 48GB GPUs CPU machine: - AMD Ryzen Threadripper PRO 3995WX 64-Cores - 512 GB RAM	N/A
ULISB	11th Gen Intel i9-11900K @ 3.5 GHz, 8 cores, RAM 128GB, GPU NVIDIA GeForce RTX 3090	

4. REFERENCES

Adler, R. F., Sapiano, M. R. P., Huffman, G. J., Wang, J.-J., Gu, G., Bolvin, D., … Ferraro, R. (2018). The Global Precipitation Climatology Project (GPCP) Monthly Analysis (New Version 2.3) and a Review of 2017 Global Precipitation. Atmosphere, 9(4), 138. https://doi.org/10.3390/atmos9040138

Baldocchi, D., Falge, E., Gu, L., Olson, R., Hollinger, D., Running, S., Wofsy, S. (2001). FLUXNET: A new tool to study the temporal and spatial variability of ecosystems–scale carbon dioxide, water vapor, and energy flux densities. Bulletin of the American Meteorological Society, 82(11), 2415–2434. https://doi.org/10.1175/1520-0477(2001)082<2415:FANTTS>2.3.CO2

Baret, F., Weiss, M., Lacaze, R., Camacho, F., Makhmara, H., Pacholcyzk, P., & Smets, B. (2013). GEOV1: LAI and FAPAR essential climate variables and FCOVER global time series capitalizing over existing products. Part1: Principles of development and production. Remote Sensing of Environment, 137, 299–309. https://doi.org/10.1016/j.rse.2012.12.027

Barriopedro, D., García-Herrera, R., Ordóñez, C., Miralles, D. G., & Salcedo-Sanz, S. (2023). Heat waves: Physical understanding and scientific challenges. Reviews of Geophysics, 61, e2022RG000780. https://doi.org/10.1029/2022RG000780

Bathiany, S., Nian, D., Drüke, M., & Boers, N. (2024). Resilience Indicators for Tropical Rainforests in a Dynamic Vegetation Model. Glob Chang Biol., 30(12):e17613. https://iopscience.iop.org/article/10.1088/1748-9326/adf7c2

Bathiany, S., Kim, E. J. & Boers, N. (2025). Multiple modes in tropical tree cover: a multi-dimensional perspective. Environmental Research Letters 20(9), 094034. doi:10.1088/1748-9326/adf7c2

Boers, N. (2021). Observation-based early-warning signals for a collapse of the Atlantic Meridional Overturning Circulation. Nature Climate Change 11, 680–688. https://doi.org/10.1038/s41558-021-01097-4

Boschetti, L., Roy, D. P., Giglio, L., Huang, H., Zubkova, M., & Humber, M. L. (2019). Global validation of the Collection 6 MODIS burned area product. Remote Sensing of Environment, 235, 111490. https://doi.org/10.1016/j.rse.2019.111490

Celesti, M. (2020). MULTI-FLEX: Towards a strategy for fluorescence monitoring at multiple scales within the context of the FLEX/S-3 tandem mission (Final report). European Space Agency

Claverie, M., Matthews, J. L., Vermote, E. F., & Justice, C. O. (2016). A 30+ year AVHRR LAI and FAPAR climate data record: Algorithm description and validation. Remote Sensing, 8(3), 263. https://doi.org/10.3390/rs8030263

Cook, E. R., & Kairiukstis, L. A. (1990). Methods of dendrochronology: Applications in the environmental sciences. Springer. https://doi.org/10.1007/978-94-015-7879-0

Copernicus Climate Change Service, Climate Data Store. (2019). Fire burned area from 2001 to present derived from satellite observation. Copernicus Climate Change Service (C3S) Climate Data Store (CDS). https://cds.climate.copernicus.eu/datasets/satellite-fire-burned-area. Retrieved on 20 July 2025

Disney, M., Muller, J.-P., Kharbouche, S., Kaminski, T., Voßbeck, M., Lewis, P., & Pinty, B. (2016). A new global fAPAR and LAI dataset derived from optimal albedo estimates: Comparison with MODIS products. Remote Sensing, 8(4), 275. https://doi.org/10.3390/rs8040275

Didan, K. (2015). MOD13A1 MODIS/Terra vegetation indices 16-day L3 global 500 m SIN grid V006 [Data set]. NASA Land Processes Distributed Active Archive Center. https://doi.org/10.5067/MODIS/MOD13A1.006. Retrieved 18 July 2025

Didan, K., Munoz, A. B., Solano, R., & Huete, A. (2015). MODIS vegetation index user's guide (MOD13 series). Vegetation Index and Phenology Lab, University of Arizona

Dorigo, W. A., Wagner, W., Albergel, C., Albrecht, F., Balsamo, G., Brocca, L., … Lecomte, P. (2017). ESA CCI Soil Moisture for improved Earth system understanding: State of the art and future directions. Remote Sensing of Environment, 203, 185–215. https://doi.org/10.1016/j.rse.2017.07.001

Drusch, M., Del Bello, U., Carlier, S., Colin, O., Fernandez, V., Gascon, F., … Bargellini, P. (2012). Sentinel-2: ESA's optical high-resolution mission for GMES operational services. Remote Sensing of Environment, 120, 25–36. https://doi.org/10.1016/j.rse.2011.11.026

European Space Agency. (2013). GlobAlbedo product user guide. European Space Agency. https://www.globalbedo.org. Retrieved 20 July 2025

European Commission – Joint Research Centre. (n.d.). Algorithms – JRC-TIP (Two-Stream Inversion Package). Publications Office of the European Union. https://fapar.jrc.ec.europa.eu/_www/algorithms.php. Retrieved 20 July 2025

EUMETSAT LSA-SAF. (n.d.). Fire Detection & Emissions: FRP-PIXEL (LSA-502). https://lsa-saf.eumetsat.int/en/data/products/fire-products/. Retrieved 28 July, 2025

EUMETSAT Navigator. (n.d.). FRP-Power Pixel (MSG) product card. https://navigator.eumetsat.int/product/EO:EUM:DAT:MSG:FRP-SEVIRI. Retrieved 28 July, 2025

EUMETSAT Satellite Application Facility on Climate Monitoring. (2024). Global Interpolated RAinFall Estimate (GIRAFE) TCDR v1.0. Copernicus Climate Data Store.

European Space Agency Climate Change Initiative (ESA CCI). (n.d.-a). Biomass—ESA Climate Change Initiative. https://climate.esa.int/en/projects/biomass/. Retrieved 25 July 2025

ESA CCI. (n.d.-b). Land Cover—ESA Climate Change Initiative. https://climate.esa.int/en/projects/land-cover/. Retrieved 25 July 2025

ESA CCI. (2022). Greenhouse Gases (GHG). https://climate.esa.int/en/projects/ghgs. Retrieved 25 July 2025

ESA CCI. (2023a). Vegetation parameters—Leaf area index and fAPAR. ESA CCI. https://climate.esa.int/en/projects/vegetation-parameters/. Retrieved on 15 June 2025

ESA CCI. (2023b). Land Surface Temperature Climate Data Record (v2.0). European Space Agency Climate Change Initiative. https://climate.esa.int/en/projects/land-surface-temperature/. Retrieved on 18 July 2025.

ESA CCI. (2024). Vegetation parameters: First data release – LAI and fAPAR dataset (2000–2020). https://climate.esa.int/en/news-events/vegetation-parameters-first-data-release/. Retrieved 18 July 2025

ESA CCI. (2025a). ESA releases the longest-ever Earth observation dataset on biomass to support forest monitoring. https://climate.esa.int/en/news-events/ESA-Releases-V6-Dataset-on-Biomass/. Retrieved on 17 July 2025

ESA CCI. (2025b). FireCCI51 Burned Area dataset (MODIS-based) for 2001–2020. European Space Agency Climate Change Initiative. https://climate.esa.int/en/projects/fire/. Retrieved on 20 July 2025

ESA CCI Biomass Team. (2023). Algorithm Theoretical Basis Document (ATBD) v4.0. ESA CCI. https://climate.esa.int/media/documents/D2_2_Algorithm_Theoretical_Basis_Document_ATBD_V4.0_20230317.pdf

ESA CCI Land Cover. (2017). Land Cover CCI Product User Guide Version 2.0. European Space Agency. https://maps.elie.ucl.ac.be/CCI/viewer/download/ESACCI-LC-Ph2-PUGv2_2.0.pdf

ESA CCI LST. (2023). Land Surface Temperature Climate Data Record (v2.0) [Data set]. European Space Agency Climate Change Initiative. https://climate.esa.int/en/projects/land-surface-temperature/. Retrieved on 18 July 2025.

ESA CCI Soil Moisture. (n.d.). ESA Soil Moisture CCI products (ACTIVE, PASSIVE, COMBINED). https://water.usgs.gov/catalog/datasets/2f3fd543-15a7-4031-8ad2-e158931f1905/. Retrieved on 20 July 2025.

Fang, H., Baret, F., Plummer, S., & Schaepman-Strub, G. (2019). An overview of global leaf area index (LAI): Methods, products, validation, and applications. Reviews of Geophysics, 57(3), 739–799. https://doi.org/10.1029/2018RG000608

Fernandez-Moran, R., Al-Yaari, A., Mialon, A., Mahmoodi, A., Al Bitar, A., De Lannoy, G., … Wigneron, J.-P. (2017). SMOS-IC: An alternative SMOS soil moisture and vegetation optical depth product. Remote Sensing, 9(5), 457. https://doi.org/10.3390/rs9050457

FLUXNET. (2020). FLUXNET data portal. https://fluxnet.org

Franquesa, M., Lizundia-Loiola, J., Stehman, S. V., & Chuvieco, E. (2022). Using long temporal reference units to assess the spatial accuracy of global satellite-derived burned area products. Remote Sensing of Environment, 269, 112823.https://doi.org/10.1016/j.rse.2021.112823

Fuster, B., Sánchez-Zapero, J., Camacho, F., García-Santos, V., Verger, A., Lacaze, R., Weiss, M., Baret, F., & Smets, B. (2020). Quality assessment of PROBA-V LAI, fAPAR and fCOVER Collection 300 m products of Copernicus Global Land Service. Remote Sensing, 12(6), 1017. https://doi.org/10.3390/rs12061017

Garrigues, S., Lacaze, R., Baret, F., Morisette, J. T., Weiss, M., Nickeson, J. E., … Yang, W. (2008). Validation and intercomparison of global Leaf Area Index products derived from remote sensing data. Journal of Geophysical Research: Biogeosciences, 113(G2). https://doi.org/10.1029/2007JG000635

Gerdener, H., Kusche, J., Schulze, K., Döll, P., & Klos, A. (2023). The global land water storage data set release 2 (GLWS2.0) derived via assimilating GRACE and GRACE-FO data into a global hydrological model. Journal of Geodesy, 97(73). https://doi.org/10.1007/s00190-023-01763-9

Giglio, L., Schroeder, W., & Justice, C. O. (2016). The Collection 6 MODIS active fire detection algorithm and fire products. Remote Sensing of Environment, 178, 31–41. https://doi.org/10.1016/j.rse.2016.02.054

Giglio, L., Boschetti, L., Roy, D. P., Humber, M. L., & Justice, C. O. (2018). The Collection 6 MODIS burned area mapping algorithm and product. Remote Sensing of Environment, 217, 72–85. https://doi.org/10.1016/j.rse.2018.08.005

Giglio, L., Schroeder, W., Hall, J.V., Justice, C.O. (2021). MODIS Collection 6 and Collection 6.1 Active Fire Product User´s Guide (v1.0). University of Maryland. NASA. https://modis-fire.umd.edu/files/MODIS_C6_C6.1_Fire_User_Guide_1.0.pdf. Retrieved 26 July 2025

Giglio, L. (2024). VIIRS/NPP Burned Area Monthly L4 Global 500 m SIN Grid V002 [Data set]. NASA Land Processes Distributed Active Archive Center. https://doi.org/10.5067/VIIRS/VNP64A1.002

Ghent, D., Anand, J. S., Veal, K., & Remedios, J. (2024). The operational and climate land surface temperature products from the Sea and Land Surface Temperature Radiometers on Sentinel-3A and 3B. Remote Sensing, 16(18), 3403. https://doi.org/10.3390/rs16183403

Ghobadi-Far, K. (2024, February 7). High-resolution terrestrial water storage changes from combination of GRACE and models. EGU Blog. https://blogs.egu.eu/divisions/g/2024/02/07/high-resolution-terrestrial-water-storage-changes-from-combination-of-grace-and-models. Retrieved on 20 July 2025

GIS StackExchange. (2022, December). Temporal analysis using SoilGrids 250m v2.0 – GEE. https://gis.stackexchange.com/questions/446701/temporal-analysis-using-soilgrids-250m-v2-0-gee. Retrieved on 20 July 2025

Global Climate Observing System (GCOS). (2024). Leaf area index (LAI). World Meteorological Organization. https://gcos.wmo.int/en/essential-climate-variables/leaf-area-index. Retrieved on 15 June 2025

Google Earth Engine Developers. (n.d.). NOAA CDR AVHRR LAI_FAPAR: Leaf Area Index and Fraction of Absorbed Photosynthetically Active Radiation, Version 5.https://developers.google.com/earth-engine/datasets/catalog/NOAA_CDR_AVHRR_LAI_FAPAR_V5. Retrieved 18 July 2025

GPCC. (2025). Global Precipitation Climatology Centre (GPCC) precipitation data products. Deutscher Wetterdienst.https://www.dwd.de/EN/research/climateenvironment/climate_monitoring/gpcc/gpcc_node.html. Retrieved 26 July 2025

GravIS. (2025). Groundwater storage anomalies. GFZ Potsdam. https://gravis.gfz-potsdam.de/gws. Retrieved on 20 July 2025

Grissino-Mayer, H. D., & Fritts, H. C. (1997). The International Tree-Ring Data Bank: An enhanced global database serving the global scientific community. The Holocene, 7(2), 235–238. https://doi.org/10.1177/095968369700700212

Grissino-Mayer, H. D. (2001). FHX2—Software for analyzing temporal and spatial patterns in fire regimes from tree rings. Tree-Ring Research, 57(1), 115–124

Gruber, A., Scanlon, T., van der Schalie, R., Wagner, W., & Dorigo, W. A. (2019). Evolution of the ESA CCI Soil Moisture Climate Data Records and their underlying merging methodology. Earth System Science Data, 11(2), 717–739. https://doi.org/10.5194/essd-11-717-2019

Güntner, A., Sharifi, E., Haas, J., Boergens, E., Dahle, C., Dobslaw, H., Dorigo, W.,…Zemp, M. (2024). Global Gravity-based Groundwater Product (G3P) v1.12. GFZ Data Services. https://doi.org/10.5880/g3p.2024.001

Hansen, M. C., Potapov, P. V., Moore, R., Hancher, M., Turubanova, S. A., Tyukavina, A., … Townshend, J. R. G. (2013). High-resolution global maps of 21st-century forest cover change. Science, 342(6160), 850–853. https://doi.org/10.1126/science.1244693

Hengl, T., Mendes de Sousa, L., Heuvelink, G. B. M., Ruiperez Gonzalez, M., Kilibarda, M., Blagotić, A.,… Kempen, B. (2017). SoilGrids250m: Global gridded soil information based on machine learning. PLOS ONE, 12(2), e0169748. https://doi.org/10.1371/journal.pone.0169748

Huete, A., Didan, K., Miura, T., Rodriguez, E. P., Gao, X., & Ferreira, L. G. (2002). Overview of the radiometric and biophysical performance of the MODIS vegetation indices. Remote Sensing of Environment, 83(1–2), 195–213. https://doi.org/10.1016/S0034-4257(02)00096-2

Humber, M. L., Boschetti, L., Giglio, L., & Justice, C. O. (2019). Spatial and temporal intercomparison of four global burned area products. International Journal of Digital Earth, 12(4), 460–484. https://doi.org/10.1080/17538947.2018.1433727

IGRAC. (2025). Global Gravity-based Groundwater Product (G3P). IGRAC (UNESCO). https://www.un-igrac.org/our-work/activities/g3p. Retrieved on 20 July 2025

INRAE. (2020/2025). SMOS-IC v2 product documentation. https://ib.remote-sensing.inrae.fr/index.php/smos-ic-v2-product-documentation. Retrieved 17 July 2025

ISRIC – World Soil Information. (n.d.). SoilGrids—global gridded soil information [Web page]. Retrieved August 13, 2025, from https://www.isric.org/explore/soilgrids. Retrieved on 20 July 2025

Joiner, J., Yoshida, Y., Vasilkov, A. P., Middleton, E. M., Campbell, P. K., Huemmrich, K. F., … Frankenberg, C. (2013). Global monitoring of terrestrial chlorophyll fluorescence from moderate-spectral-resolution near-infrared satellite measurements: methodology, simulations, and application to GOME-2. Atmospheric Measurement Techniques, 6(10), 2803–2823. https://doi.org/10.5194/amt-6-2803-2013

Kidwell, K. B. (1998). NOAA polar orbiter data users guide. NOAA/NESDIS.

Knyazikhin, Y., Martonchik, J.V., Diner, D.J., Myneni, R.B., Verstraete, M.M., Pinty, B., and Gobron, N. (1998a). Estimation of vegetation canopy leaf area index and fraction of absorbed photosynthetically active radiation from atmosphere-corrected MISR data. Journal of Geophysical Research 103(D24), 32239-32256. https://doi.org/10.1029/98JD02461

Knyazikhin, Y., Martonchik, J.V., Myneni, R.B., Diner, D.J. Running, S.W. (1998b). Synergistic algorithm for estimating vegetation canopy leaf area index and fraction of absorbed photosynthetically active radiation from MODIS and MISR data. Journal of Geophysical Research 103(D24), 32257-32275.https://doi.org/10.1029/98JD02462

Konings, A. G., Rao, K., and Steele-Dunne, S. C. (2019). Macro to micro: microwave remote sensing of plant water content for physiology and ecology, New Phytol., 223, 1166–1172. https://doi.org/10.1111/nph.15808

Köhl, M., Magnussen, S. S., & Marchetti, M. (2006). Sampling methods, remote sensing and GIS multiresource forest inventory. Springer-Verlag. https://doi.org/10.1007/978-3-540-32572-7

Köhler, P., Guanter, L., & Joiner, J. (2015). A linear method for the retrieval of sun-induced chlorophyll fluorescence from GOME-2 and SCIAMACHY data. Atmospheric Measurement Techniques, 8(6), 2589–2608. https://doi.org/10.5194/amt-8-2589-2015

LAADS DAAC. (n.d.). VNP14IMG—VIIRS/NPP Active Fires (375 m) product page. https://ladsweb.modaps.eosdis.nasa.gov/missions-and-measurements/products/VNP14IMG/. Retrieved 28 July 2025

Landerer, F., Flechtner, F., Save, H., McCullough, C., Dahle, C., Bettadpur, S., Gaston, R., Snopek, K., and Reager, J. T. (2024). GRACE-FO: science results, mission status and outlook, GRACE/GRACE-FO Science Team Meeting, Potsdam, Germany, 8–10 Oct 2024, GSTM2024-94, https://doi.org/10.5194/gstm2024-94

Li, W., MacBean, N., Ciais, P., Defourny, P., Lamarche, C., Bontemps, S., Houghton, R. A., Peng, S. (2018). Gross and net land cover changes in the main plant functional types derived from the annual ESA CCI land cover maps (1992–2015). Earth System Science Data, 10(1), 219–234. https://doi.org/10.5194/essd-10-219-2018

Li, X., Wigneron, J.-P., Fan, L., Frappart, F., Yueh, S., Colliander, A.,…Ciais, P. (2022). A new SMAP soil moisture and vegetation optical depth product (SMAP-IB): Algorithm, assessment and intercomparison. Remote Sensing of Environment, 271: 112921. https://doi.org/10.1016/j.rse.2022.112921

Lizundia-Loiola, J., Otón, G., Ramo, R., & Chuvieco, E. (2020). A spatio-temporal active-fire clustering approach for global burned area mapping at 250 m from MODIS data. Remote Sensing of Environment, 236, 111493. https://doi.org/10.1016/j.rse.2019.111493

LP DAAC. (2019). Collection 1 VIIRS Burned Area Product User´s Guide. NASA LP DAAC. Retrieved from https://lpdaac.usgs.gov/documents/1330/VNP64A1_User_Guide_V1.pdf. Retrieved 12 August 2025

LP DAAC. (2021). MCD64A1 v6.1 User Guide; product page/DOI: 10.5067/MODIS/MCD64A1.061. Retrieved 12 August 2025

MacDicken, K. (2015). Global Forest Resources Assessment 2015: what, why and how? Forest Ecology and Management, 352, 3–8. https://doi.org/10.1016/j.foreco.2015.02.006

Main-Knorn, M., Pflug, B., Louis, J., Debaecker, V., Müller-Wilm, U., & Gascon, F. (2017). Sen2Cor for Sentinel-2. Proc. of the Living Planet Symposium 2016, 740. https://elib.dlr.de/117678/1/1042704_Main-Knorn_et_al.pdf

Mahowald, N., Lo, F., Zheng, Y., Harrison, L., Funk, C., Lombardozzi, D., & Goodale, C. (2016). Projections of leaf area index in Earth system models. Earth System Dynamics, 7(1), 211–229. https://doi.org/10.5194/esd-7-211-2016

Margolis, E. Q., Guiterman, C. H., Chavardès, R., Coop, J.D., Copes-Gerbitz, K., Dawe, D.A.,…Weisberg, P.J. (2022). The North American tree-ring fire-scar network. Ecosphere*, 13*, e4159. https://doi.org/10.1002/ecs2.4159

Mialon, A., Rodríguez-Fernández, N. J., Santoro, M., Saatchi, S., Mermoz, S., Bousquet, E., & Kerr, Y. H. (2020). Evaluation of the Sensitivity of SMOS L-VOD to Forest Above-Ground Biomass at Global Scale. Remote Sensing, 12(9), 1450. https://doi.org/10.3390/rs12091450

Moesinger, L., Dorigo, W., de Jeu, R., van der Schalie, R., Scanlon, T., Teubner, I., & Forkel, M. (2020). The global long-term microwave Vegetation Optical Depth Climate Archive (VODCA). Earth System Science Data, 12(1), 177–196. https://doi.org/10.5194/essd-12-177-2020

Moesinger, L., Zotta, R.-M., van der Schalie, R., Scanlon, T., de Jeu, R., & Dorigo, W. (2022a). Monitoring vegetation condition using microwave remote sensing: The standardized vegetation optical depth index (SVODI). Biogeosciences, 19(21), 5107–5123. https://doi.org/10.5194/bg-19-5107-2022

Moesinger, L., Zotta, R.-M., van der Schalie, R., Scanlon, T., de Jeu, R., & Dorigo, W. (2022b). The Standardized Vegetation Optical Depth Index SVODI [Data set]. Zenodo. https://doi.org/10.5281/zenodo.7114654

Mota, B., Gobron, N., Morgan, O., Cappucci, F., Lanconelli, C., Robustelli, M. (2021). Cross-ECV consistency at global scale: LAI and FAPAR changes. Remote Sensing of Environment 263, 112561. https://doi.org/10.1016/j.rse.2021.112561

Myneni, R. B., Hall, F. G., Sellers, P. J., & Marshak, A. L. (1995). The interpretation of spectral vegetation indexes. IEEE Transactions on Geoscience and Remote Sensing, 33(2), 481–486. https://doi: 10.1109/TGRS.1995.8746029

Myneni, R. B., Knyazikhin, Y., & Park, T. (2015). MCD15A2H MODIS/Terra+Aqua Leaf Area Index/FPAR 8-Day L4 Global 500m SIN Grid V006 [Data set]. NASA EOSDIS Land Processes DAAC. https://doi.org/10.5067/MODIS/MCD15A2H.006. Retrieved 22 July 2025

Muñoz-Sabater, J., Dutra, E., Agustí-Panareda, A., Albergel, C., Arduini, G., Balsamo, G., …Thépaut, J.-N. (2021). ERA5-Land: A state-of-the-art global reanalysis dataset for land applications. Earth System Science Data, 13(9), 4349–4383. https://doi.org/10.5194/essd-13-4349-2021

NASA JPL. (n.d.). JPL GRACE and GRACE-FO Mascon Ocean, Ice and Hydrology Equivalent Water Height Coastal Resolution Improvement (CRI) Filtered Release 06.3 Version 04. https://podaac.jpl.nasa.gov/dataset/TELLUS_GRAC-GRFO_MASCON_CRI_GRID_RL06.3_V4. Retrieved on 20 July 2025

NASA FIRMS. (2024). MODIS active fire descriptions and archive access. https://firms.modaps.eosdis.nasa.gov. Access 26 July 2025

NASA VIIRS Land Team. (n.d.). Active fire product overview. https://viirsland.gsfc.nasa.gov/Products/NASA/FireESDR.html. Retrieved 28 July 2025

NOAA NCEI. (2019). NOAA Climate Data Record (CDR) of AVHRR Surface Reflectance, Version 5. NOAA National Centers for Environmental Information. https://doi.org/10.7289/V53776Z4. Retrieved 18 July 2025

NOAA NCEI. (2023). International Tree-Ring Data Bank (ITRDB) [Data set]. National Centers for Environmental Information. https://www.ncei.noaa.gov/products/paleoclimatology/tree-ring

NOAA NCEI (2024). North American Tree-ring Fire-Scar Synthesis (NAFSS) https://www.ncei.noaa.gov/access/metadata/landing-page/bin/iso?id=noaa-fire-34853

Oliveira, S. L. J. , Pereira, J. M. C. , Carreiras, J. M. B. (2011). Fire frequency analysis in Portugal (1975-2005), using Landsat-based burnt area maps. International Journal Wildland Fire, 21:48–60. https://doi.org/10.1071/WF10131

O'Neill, C., & Chandler-Ho, S. (2021). Decreasing water budget of the Australian continent from GRACE satellite gravity data. Earth Science Preprint. https://arxiv.org/abs/2101.11167

Otón, G., Pereira, J. M. C., Silva, J. M. N., & Chuvieco, E. (2021). Analysis of trends in the FireCCI Global Long-Term Burned Area Product (1982–2018). Fire, 4(4), 74. https://doi.org/10.3390/fire4040074

Owe, M., de Jeu, R. A. M., & Holmes, T. R. H. (2008). Multisensor historical climatology of satellite-derived global land surface moisture. Journal of Geophysical Research: Earth Surface, 113(F1), F01002. https://doi.org/10.1029/2007JF000769

Pastorello, G., Trotta, C., Canfora, E., Chu, H., Christianson, D., Cheah, Y.-W., … Papale, D. (2020). The FLUXNET2015 dataset and the ONEFlux processing pipeline for eddy covariance data. Scientific Data, 7(1), 225. https://doi.org/10.1038/s41597-020-0534-3

Pinty ,B., Lavergne, T., Dickinson, R.E., Widlowski, J. -L., Gobron, N., Verstraete, M.M. (2006). Simplifying the interaction of land surfaces with radiation for relating remote sensing products to climate models. J. Geophys. Res., 111. https://doi.org/10.1029/2005JD005952

Pinzon, J. E., & Tucker, C. J. (2014). A non-stationary 1981–2012 AVHRR NDVI3g time series. Remote Sensing, 6(8), 6929–6960. https://doi.org/10.3390/rs6086929

Preimesberger, W., Scanlon, T., Su, C.-H., Gruber, A., & Dorigo, W. (2021). Homogenization of structural breaks in the global ESA CCI Soil Moisture multi-satellite climate data record. IEEE Transactions on Geoscience and Remote Sensing, 59(4), 2845–2862. https://doi.org/10.1109/TGRS.2020.3012896

Reuter, M., Buchwitz, M., Schneising, O., Noël, S., Rozanov, V., Bovensmann, H., & Burrows, J. P. (2017). A Fast Atmospheric Trace Gas Retrieval for Hyperspectral Instruments Approximating Multiple Scattering—Part 2: Application to XCO_2 Retrievals from OCO-2. Remote Sensing, 9(11), 1102. https://doi.org/10.3390/rs9111102

Reuter, M., Hilker, M., Noël, S.; Buchwitz, M., Schneising, O., Bovensmann, H., Burrows, J.P. (2023). ESA Greenhouse Gases Climate Change Initiative (GHG_cci): Column averaged carbon dioxide from OCO-2 generated with the FOCAL algorithm, version 10. NERC EDS Centre for Environmental Data Analysis, 17 January 2023. https://dx.doi.org/10.5285/070522ac6a5d4973a95c544beef714b4

Roberts, G., Wooster, M. J., Freeborn, P. H., Morcrette, J.J., Jones, L.,… Kaiser, J.W. (2015). LSA SAF Meteosat FRP products—Part 2: Evaluation and demonstration for use in the Copernicus Atmosphere Monitoring Service (CAMS). Atmospheric Chemistry and Physics, 15, 13241–13267. https://doi.org/10.5194/acp-15-13241-2015

Roy, D. P., Wulder, M. A., Loveland, T. R., Woodcock, C. E., Allen, R. G., Anderson, M. C., … Zhu, Z. (2014). Landsat-8: Science and product vision for terrestrial global change research. Remote Sensing of Environment, 145, 154–172. https://doi.org/10.1016/j.rse.2014.02.001

Santoro, M., Cartus, O., Carvalhais, N., Rozendaal, D. M. A., Avitabile, V., Araza, A., … Willcock, S. (2021). The global forest above-ground biomass pool for 2010 estimated from high-resolution satellite observations. Earth System Science Data, 13(9), 3927–3950. https://doi.org/10.5194/essd-13-3927-2021

Santoro, M. (2024). CCI Biomass Product Fact Sheet v5.0. ESA CCI. https://climate.esa.int/documents/2791/CCI_Biomass_product_fact_sheet_V5.0_20240319.pdf

Santoro, M., & Cartus, O. (2025). ESA Biomass CCI: Global datasets of forest above-ground biomass for 2007, 2010, 2015–2022 (v6.0) [Data set]. CEDA. https://doi.org/10.5285/95913ffb6467447ca72c4e9d8cf30501

Seguini, L., Klisch, A., Meroni, M., Vrieling, A., Manfron, G., Atzberger, C., and Rembold, F. (2025). Global near real-time 500 m 10-day FPAR dataset from MODIS and VIIRS for operational agricultural monitoring and crop yield forecasting, Earth Syst. Sci. Data Discuss. [preprint], https://doi.org/10.5194/essd-2025-287, in review.

Schamm, K., Ziese, M., Becker, A., Finger, P., Meyer-Christoffer, A., Schneider, U., Schröder, M., & Stender, P. (2014). Global gridded precipitation over land: a description of the new GPCC First Guess Daily product. Earth System Science Data, 6(1), 49–60. https://doi.org/10.5194/essd-6-49-2014

Schroeder, W., Oliva, P., Giglio, L., & Csiszar, I. A. (2014). The new VIIRS 375 m active fire detection product: Algorithm description and initial assessment. Remote Sensing of Environment, 143, 85–96. https://doi.org/10.1016/j.rse.2013.12.008

Schroeder, W., Giglio, L., Hall, J. (2024). Collection 2 Visible Infrared Imaging Radiometer Suite (VIIRS) 375-m Active Fire Product User's Guide (v1.0). NASA. https://ladsweb.modaps.eosdis.nasa.gov/archive/Document%20Archive/Science%20Data%20Product%20Documentation/VIIRS_C2_AF-375m_User_Guide_1.0.pdf. Retrieved 26 July 2025

Schneider, U., Hänsel, S., Finger, P., Rustemeier, E., & Ziese, M. (2022). GPCC Full Data Monthly Product Version 2022 (at 0.25° at 0.5°, 1.0°, 2.5°): Monthly land-surface precipitation from rain gauges built on GTS-based and historic data. https://doi.org/10.5676/DWD_GPCC/FD_M_V2022_250

Schmidt, L., Forkel, M., Zotta, R.-M., Scherrer, S., Dorigo, W. A., Kuhn-Régnier, A.,…Yebra, M. (2023). Assessing the sensitivity of multi-frequency passive microwave vegetation optical depth to vegetation properties, Biogeosciences, 20, 1027–1046, https://doi.org/10.5194/bg-20-1027-2023

Shekhar, A., Buchmann, N., Gharun, M. (2022). How well do recently reconstructed solar-induced fluorescence datasets model gross primary productivity? Remote Sensing of Environment, 283, 113282. https://doi.org/10.1016/j.rse.2022.113282

Sims, M. J., Stanimirova, R., Raichuk, A., Neumann, M., Richter, J., Follett, F., … Harris, N. (2025). Global drivers of forest loss at 1 km resolution. Environmental Research Letters, 20(7), 074027. https://doi.org/10.1088/1748-9326/add606

Skulovich, O., Gentine, P., Wigneron, J.-P., & Xiaojun, L. (2023). GLAB-VOD: Global L-band AI-Based Vegetation Optical Depth Dataset Based on Machine Learning and Remote Sensing (V1.0) [Data set]. Zenodo. https://doi.org/10.5281/zenodo.10306095

Skulovich, O., Li, X., Wigneron, J.-P., & Gentine, P. (2024). Global L-band equivalent AI-based vegetation optical depth dataset (GLAB-VOD). Scientific Data, 11, 936. https://doi.org/10.1038/s41597-024-03810-2

Smith, T., Traxl, D. & Boers, N. (2022). Empirical evidence for recent global shifts in vegetation resilience. Nature Climate Change 12, 477–484. https://doi.org/10.1038/s41559-023-02194-7

Sun, Y., Frankenberg, C., Jung, M., Joanna, J., Guanter, L., Kohler, P., Magney, T.S. (2018). Overview of Solar-Induced chlorophyll Fluorescence (SIF) from the Orbiting Carbon Observatory-2: Retrieval, cross-mission comparison, and global monitoring for GPP. Remote Sensing of Environment, 209, 808–823. https://doi.org/10.1016/j.rse.2018.02.016

Swinnen, E., Van der Tol, C., Blessing, S., Camacho, F., Giering, R., Jolivet, D., … Vanhoof, K. (2023). ESA Vegetation Parameters Climate Change Initiative (Vegetation_Parameters_cci): LAI and fAPAR, Version 1.0. Centre for Environmental Data Analysis. https://doi.org/10.5285/34e4bfe402c048c783e64eac0f0bca37. Retrieved 18 July 2025

Tao, S., Chave, J., Frison, P., Le Toan, T., Ciais, P., Fang, J.,…Saatchi, S. (2022). Increasing and widespread vulnerability of intact tropical rainforests to repeated droughts. Proceedings of the National Academy of Sciences of the United States of America, 119(37), e2116626119. https://doi.org/10.1073/pnas.2116626119

Tao, S., Ao, Z., Wigneron, J.-P., Saatchi, S., Ciais, P., Chave, J.,...Fang, J. (2023). A global long-term, high-resolution satellite radar backscatter data record (1992–2022+): Merging C-band ERS/ASCAT and Ku-band QSCAT. Earth System Science Data, 15, 1577–1596. https://doi.org/10.5194/essd-15-1577-2023

Tomppo, E., Gschwantner, T., Lawrence, M., & McRoberts, R. E. (Eds.). (2010). National forest inventories: Pathways for common reporting. Springer. https://doi.org/10.1007/978-90-481-3233-1

Tucker, C. J., Pinzon, J. E., Brown, M. E., Slayback, D. A., Pak, E. W., Mahoney, R., … El Saleous, N. (2005). An extended AVHRR 8-km NDVI dataset compatible with MODIS and SPOT vegetation NDVI data. International Journal of Remote Sensing, 26(20), 4485–4498. https://doi.org/10.1080/01431160500168686

Verger, A., Baret, F., & Weiss, M. (2014). Near real-time vegetation monitoring at global scale. IEEE Journal of Selected Topics in Applied Earth Observations and Remote Sensing, 7(8), 3473–3481. https://doi.org/10.1109/JSTARS.2014.2328632

UCAR Climate Data Guide. (2025). GPCP (Monthly): Global Precipitation Climatology Project. https://climatedataguide.ucar.edu/climate-data/gpcp-monthly-global-precipitation-climatology-project. Retrieved August 2, 2025

USGS. (2019). Landsat surface reflectance product guide. U.S. Geological Survey. https://www.usgs.gov/core-science-systems/nli/landsat. Retrieved 20 July 2025

U.S. Data.gov. (2024). *North American tree-ring fire-scar site descriptions*. https://catalog.data.gov/dataset/north-american-tree-ring-fire-scar-site-descriptions. Retrieved 28 July 2025

Vermote, E., Justice, C., Claverie, M., & Franch, B. (2016). Preliminary analysis of the performance of the Landsat 8/OLI land surface reflectance product. Remote Sensing of Environment, 185, 46–56. https://doi.org/10.1016/j.rse.2016.04.008

Vermote, E., & NOAA CDR Program. (2019a). NOAA Climate Data Record (CDR) of AVHRR Leaf Area Index (LAI) and Fraction of Absorbed Photosynthetically Active Radiation (FAPAR), Version 5. NOAA National Centers for Environmental Information. https://doi.org/10.7289/V5TT4P69. Retrieved 18 July 2025

Vermote, E., NOAA CDR Program. (2019b). NOAA Climate Data Record (CDR) of AVHRR Normalized Difference Vegetation Index (NDVI), Version 5. NOAA National Centers for Environmental Information. https://doi.org/10.7289/V5ZG6QH9. Retrieved 20 July 2025

Wigneron, J.-P., Li, X., Frappart, F., Fan, L., Al-Yaari, A., De Lannoy, G., … Moisy, C. (2021). SMOS-IC data record of soil moisture and L-VOD: Historical development, applications and perspectives. Remote Sensing of Environment, 254, 112238. https://doi.org/10.1016/j.rse.2020.112238

Wooster, M.J., Zhukov, B., Oertel, D. (2003). Fire radiative energy for quantitative study of biomass burning: derivation from the BIRD experimental satellite and comparison to MODIS fire products. Remote Sensing of Environment, 86,83-107. https://doi.org/10.1016/S0034-4257(03)00070-1

Wooster, M. J., Roberts, G., Perry, G. L. W., & Kaufman, Y. J. (2005). Retrieval of biomass combustion rates and totals from fire radiative power observations: FRP derivation and calibration relationships between biomass consumption and fire radiative energy release. Journal of Geophysical Research: Atmospheres, 110, D24. https://doi.org/10.1029/2005JD006318

Wooster, M. J., Roberts, G., Freeborn, P. H., Xu, W., Govaerts, Y., Beeby, R.,…Mullen, R. (2015). LSA SAF Meteosat FRP products—Part 1: Algorithms, product contents, and analysis. Atmospheric Chemistry and Physics, 15, 13217–13239. https://doi.org/10.5194/acp-15-13217-2015

Wulder, M. A., Roy, D. P., Radeloff, V. C., Loveland, T. R., Anderson, M. C., Johnson, D. M., … Cook, B. D. (2022). Fifty years of Landsat science and impacts. Remote Sensing of Environment, 228, 164–183. https://doi.org/10.1016/j.rse.2022.113195

Yang, W., Huang, D., Tan, B., Stroeve, J. C., Shabanov, N. V., Knyazikhin, Y., … Myneni, R. B. (2006). Analysis of leaf area index and fraction of PAR absorbed by vegetation products from the Terra

MODIS sensor: 2000–2005. IEEE Transactions on Geoscience and Remote Sensing, 44(7), 1829–1842. https://doi.org/10.1109/TGRS.2006.871214

Zhang, Y., Joiner, J., Alemohammad, S. H., Zhou, S., & Gentine, P. (2018). A global spatially contiguous solar-induced fluorescence (CSIF) dataset using neural networks. Biogeosciences, 15, 5779–5800. https://doi.org/10.5194/bg-15-5779-2018

Zhang, Y. (2018). CSIF. figshare. Dataset. https://doi.org/10.6084/m9.figshare.6387494.v2

Zhu, Z., & Woodcock, C. E. (2014). Continuous change detection and classification of land cover using all available Landsat data. Remote Sensing of Environment, 144, 152–171. https://doi.org/10.1016/j.rse.2014.01.011

Zotta, R.-M., Moesinger, L., van der Schalie, R., Vreugdenhil, M., Preimesberger, W., Frederikse, T., de Jeu, R., & Dorigo, W. (2024). VODCA v2: multi-sensor, multi-frequency vegetation optical depth data for long-term canopy dynamics and biomass monitoring. Earth System Science Data, 16(10), 4573–4617. https://doi.org/10.5194/essd-16-4573-2024

Zotta, R.-M., de Jeu, R., Bader, N. F., Frederikse, T., & Dorigo, W. (2025). Improving vegetation optical depth estimates from AMSR2 by optimising the parametrisation of the Land Parameter Retrieval Model. Manuscript in review at Remote Sensing of Environment